Stony Brook University

STIRAP on Helium: Excitation to Rydberg States

A Thesis presented

by

Deqian Yuan

to

The Graduate School

in Partial Fulfillment of the

Requirements

for the Degree of

Master of Arts

in

Physics

Stony Brook University

May 2015

Stony Brook University

The Graduate School

Deqian Yuan

We, the thesis committe for the above candidate for the

Master of Arts degree, hereby recommend

acceptance of this thesis

Harold Metcalf - Thesis Advisor
Distinguished Teaching Professor, Department of Physics and Astronomy

Eden Figueroa - Chairperson of Defense
Assistant Professor, Department of Physics and Astronomy

Dmitri Averin
Professor, Department of Physics and Astronomy
length.

This thesis is accepted by the Graduate School

Charles Taber
Dean of the Graduate School

Abstract of the Thesis

STIRAP on Helium: Excitation to Rydberg States

by

Deqian Yuan

Master of Arts

in

Physics

Stony Brook University

2014

Research in optically induced transitions between different atomic levels has a long history. For transitions between states driven by a coherent optical field, the theoretical efficiency could be ideally high as 100% but there could be many factors preventing this. In the three state helium atom excitation process, i.e. $2^3\mathrm{S} \rightarrow 3^3\mathrm{P} \rightarrow n\mathrm{L}$, the stimulated emission from intermediate state makes it hard to achieve efficient population transfer to the final state through an intuitive excitation order. One technique to achieve a higher efficiency is Stimulated Raman Adiabatic Passage (STIRAP) which is being studied and under research in our lab. Unlike traditional three level excitation processes, STIRAP actually uses a counter intuitive pulsed laser beams timing arrangement.

The excitation objects are metastable helium atoms traveling in a vacuum system with a longitudinal velocity of $\sim$ 1070 m/s. We are using a 389 nm UV laser to connect the $2^3\mathrm{S}$ and the $3^3\mathrm{P}$ state and a frequency tunable $\sim$ 790 nm

IR laser to connect the 3^3P state and the different Rydberg states.

A third 1083 nm wavelength laser beam drives the $2^3\text{S} \rightarrow 2^3\text{P}$ transition to transversely separate the residual metastable atoms and the Rydberg atoms for efficiency measurements. The data is taken by a stainless steel detector in the vacuum system.

As the Rydberg atoms will get ionized by blackbody radiation under room temperature, we can utilize this for their detection. An ion detector sitting on the field plate is capable to collect the ion signals of the Rydberg atoms for detection.

So far the whole system has not been ready for data collection and measurement, so here we are using data and results from previous theses for discussions. The highest transition frequency that has ever been achieved in our lab is around 70% after corrections.

For my family

and my love Xiwu

Contents

List of Figures

List of Tables

Acknowledgements

I have been in Stony Brook University for two years and working in Prof. Metcalf's group for about one year. During this time it has always been a great pleasure for me to work alongside so many great people. The work in this thesis is based on a lot of people's help and instructions. Here I would like to thank the authors of the previous theses that I used the information provided in: Xiaoxu Lu, Yuan Sun, and Seung Hyun Lee.

Graduating as a Master student, I first want to express my utmost gratitude and respect to my instructor Prof. Harold Metcalf. He has provided a lot of support and help during the time I am here. Even if I leave here, I will always remember everything he has done for me. Thank you, Hal.

I appreciate all the help I have received from the colleagues in this group. The people I have been working with: Mr. Zakharov, Mr. Arnold, Mr. Elgin, Dr. Corder, Mr. McKenna, and Ms. Gasparik. It has always been a pleasure to receive help from, to work with, and to know you guys. Love you all.

I am also grateful to my family: my parents, my aunt, and my cousin. It is the love from you that drives me to improve. I feel I am among the luckiest to have a family like you guys.

Many thanks to my friends in both China and the United States, especially

my buddy Zale Qu. Working as a graduate student is not easy. There have been hard times and depressions. Thank you for all the support and trust to help me make through.

Finally I would like to thank my loving girlfriend Xiwu. Working at Stony Brook for these two years makes me a better physicist, but knowing and being together with you makes me a better person. It has not been always easy. Thank you for the support, my love. I love you.

Salute.

Chapter 1

Introduction

1.1 General Background

In the present era of AMO physics, the manipulation of atom beams using optical fields has been a major topic for a long time. Great interests and efforts have been put into the optical manipulation of the motion of atoms and the study of light-matter interaction. Exploring the wave properties of particles and utilizing it is one of the keys to the subject. The history of using a field to manipulate a particle beam can begin as early as the famous Stern and Gerlach's experiment in the 1920s which was later followed by Estermann [1] and others in the early 1930s. In their experiments great demonstrations about properties of atoms were made, and the topic of atom optics has been brought to uncover since then.

In the late 1970s, Hänsch and Schawlow proposed that using the laser ra-

diation force, one can achieve the cooling of an atomic gas [2]. More than two decades after that, the idea of cooling atomic gas finally led to the Nobel Prize in 1997 of laser cooling. The temperature of the atomic sample can be brought down as low as 10^{-6} K or even lower. This means the wavelength of the de Broglie matter wave is now readily on the order of microns [3]. The laser cooling technique actually led to the very first creation of Bose-Einstein condensates in a dilute gas of alkali atoms [4].

With appropriate laser wavelengths, atomic beams can be reflected [5], diffracted [3], and focussed [6]. These phenomena all proved that we can transfer momentum and energy to atoms through the interaction between atoms and light. However, due to the small electric dipole moments of neutral atoms, it is really hard to transfer momentum to and manipulate these atoms, and to do so, huge field intensities are needed [7]. One may ask: Can atoms with larger electric dipole moments be created and used as the candidates of laser cooling? The question could be solved by the Rydberg atoms with large electric dipole moments because of their high quantum numbers.

After the discovery and demonstration of Rydberg-Rydberg blockade phenomenon [8], Rydberg atoms have become an ideal candidate of optical manipulation [9] because they have large electric dipole moments as we will introduce in the next section. Rydberg atoms need to be created by a special method which allows us to maximize the creation efficiency.

In our lab, several previous researchers have done excellent work in the research of Stimulated Raman Adiabatic Passage (STIRAP) technique and the

results are reported in their Ph.D. theses [10] [11] [12]. Before we start discussing the technique, let's first take a look at the Rydberg atoms themselves.

1.2 Rydberg Atoms

1.2.1 History

A Rydberg atom is defined as *an excited atom with one or more electrons that have a high principle quantum number* [13]. The existence of Rydberg series was first demonstrated when Balmer proposed a formula in 1885, which is later named after him, that describes the wavelengths of the spectral line emissions in the hydrogen atomic system [13]

$$\lambda = B(\frac{n^2}{n^2 - 4}) \tag{1.1}$$

in which B is known as Balmer's constant for $B \approx 3645\mathring{A}$ and n is the quantum state number. Three years later Swedish physicist J. Rydberg re-expressed Balmer's formula in a more intuitive version which is known to us as the Rydberg formula in 1888. At that time he was working to describe the wavelengths of spectral lines of alkali atoms. Rydberg proposed that there could be certain associations between spectral lines of different series, and he noticed that the lines came in series could be simplified by using the measurement of wavenumber. He plotted the wavenumbers of successive lines from different series of alkali atoms and the resulting curves were similar and seemed to fit a single function. The constant terms in the formula he proposed for a certain series

had the same value as the first running term n_0 in other series. After becoming aware of Balmer's result on hydrogen atom, he rewrote Balmer's formula and suggested it should be a special case of the formula which is later known as the famous Rydberg formula [14]

$$k = k_0 - \frac{R_y}{(n - \delta_l)^2} \tag{1.2}$$

R_y is the universal Rydberg constant for Rydberg discovered that the constant applies to all kinds of atoms, k is the wavenumber and k_0 is the series limit. Here δ_l is the quantum defect term in atoms other than hydrogen. The Rydberg formula indicated the existence of an infinite series of even more closely spaced discrete energy levels converging on a finite limit k_0 as the wavenumber approaches it [14]. For the specific case of hydrogen (the wavenumber form of Balmer's formula):

$$k = \frac{1}{\lambda} = R_y(1/4 - 1/n^2) \tag{1.3}$$

Comparing it to equation 2, we see this should be a special case of $\delta_l = 0$ and $R_y = 4k_0$. Here $k_0 = 1/B$, the reciprocal of Balmer's constant.

Quantum states with the energy that follows Rydberg formula are known as Rydberg states. In general, an excited electron and ionic core system, with a sufficiently high principle quantum number, will satisfy the Rydberg formula and have the similar properties to a hydrogen atom [13] (and is considered as a Rydberg atom now). At that time people were not clear about the reason of

this.

After Bohr proposed his hydrogen atomic model in 1913, everything seemed to make sense. As the Bohr model exposed, the electron orbit radius should scale with n^2, we see Rydberg atoms with high principle quantum numbers have significantly large radii that the inner electrons will shield the outer ones from the nucleus and this brings along a lot of peculiar properties and some of them will be introduced in this chapter. Because of the special properties that ground state atoms would not have, Rydberg atoms have attracted the attention of researchers for more than a century. It is the goal of the STIRAP excitation experiment as we are about to introduce.

In general, to produce Rydberg atoms, one can use electron impact excitation [15], charge exchange excitation [16], or optical excitation. As inelastic scattering happens when an electron beam hits the ground state atoms, the kinetic energy that the electrons carry could excite the ground state atoms to a broad range of different states including high energy Rydberg states; Electrons from neutral atoms can be captured by an ion beam when the ion beam hits the atom beam, leaving it into the excited states; The optical excitation, because it allows control on a greater level and the access to the exact Rydberg state, has become the major tool for atom excitation.

1.2.2 General Properties of Rydberg Atoms

We mentioned that as the orbit radius of Rydberg atoms is so large ($\propto n^2$) that it brings along a lot of unique properties. As in table 1.1, parameters

including binding energy and energy spacing will all respond to the large radius.

Property	Formula	n-dependence
Binding Energy	$-\frac{R_y}{(n-\delta_l)^2}$	n^{-2}
Energy Spacing	$E_n - E_{n-1}$	n^{-3}
Orbital Radius	$\sim \frac{3(n-\delta_l)^2 - l(l+1)}{2} a_0$	n^2
Dipole Moment	$\langle nl\|er\|nl+1\rangle$	n^2
Geo. Cross Section	$\pi \langle r \rangle^2$	n^4
Polarizability	$2e^2 \sum_{n=n',l,m} \frac{\|\langle nlm\|z\|n'l'm'\rangle\|^2}{E_{nlm} - E_{n'l'm'}}$	n^7
Radiative Lifetime	$1/(\frac{e^2}{3\hbar c^3 \pi \epsilon_0} \sum_{n<n'}^{l=l\pm1} \frac{l_{max}}{2l'+1} \omega^3 \|\langle n'l'\|r\|nl\rangle\|^2)$	n^{-3}
Blackbody Transition	$\frac{1}{\tau_{nl}^{bb}} = \frac{4\alpha^3 kT}{3n^2}$	n^{-2}

Table 1.1: Some atomic parameters of Rydberg atoms related to n [17]. Due to the large radius some of these parameters could bring interesting properties.

As the Rydberg atomic radius is so large and the neighboring states sit so close with each other, a BBR (black body radiation) field is capable of causing a transition between states. The BBR can also ionize the Rydberg atoms as the electrons are so loosely bound in the orbit and reduce the lifetime of Rydberg atoms.

The dipole moments of Rydberg atoms are very large and this will lead to a distinct Stark effect in the Rydberg atoms when there is an external electric field. The spectral lines of high lying state atoms will split at the presence of

modest external fields. This allows us to use lasers with different wavelengths to connect the ground state to different Rydberg states with or without an external field.

As we mentioned above, the inner electrons block the outer ones to "see" the nucleus that the Rydberg atoms behave like a hydrogen atom. But as the low-lying outer electrons for multi-electron Rydberg atoms may polarize or penetrate the inner core [18], from the point of view from the outer electrons, the ionic core will "look" like a hydrogen core to them. This is known as the quantum defect phenomenon.

In the following section we will mainly discuss these two major structural properties (quantum defect and Stark effect) of Rydberg atoms.

1.2.3 Quantum Defect

If we look at a hydrogen atom, the energy levels dependent on quantum number n could be easily obtained: $E_n = -\frac{R_y}{(n)^2}$ where R_y is the Rydberg constant. The energy here is proportional to n^{-2} and we should expect Rydberg atoms to behave similarly due to their properties. But as in equation 1.2, the calculated wavenumber result has a δ_l term which will be induced to the energy. This is known the quantum defect. Here the electron with low angular momentum will occasionally "see" the whole nucleus and the other electrons, and the binding energy here can be written as [19]

$$E_n = -\frac{R_y}{(n-\delta_l)^2} \tag{1.4}$$

Element	Configuration	$n - \delta_s$	δ_s
Li	2S	1.59	0.41
Na	3S	1.63	1.37
K	4S	1.77	2.23
Rb	5S	1.81	3.19
Cs	6S	1.87	4.13

Table 1.2: Quantum defect for alkali metal in the S states [19].

where the quantum defect term is independent of principle quantum number n but depends on the angular quantum number l. We may express the quantum defect term by Rydberg-Ritz formula [20]

$$\delta_l = a + bE_n + cE_n{}^2 + dE_n{}^3 + ... \tag{1.5}$$

where $a, b, c, d...$ are the Rydberg-Ritz coefficients. They each depends on the angular momentum l. For alkali metal atoms in the S states, their quantum defects are shown in table 1.2.

The Rydberg-Ritz coefficients for triplet helium atoms are shown in table 1.3 as an example since we are using helium atoms as our experiment object.

Ang. momentum l	a	b	c	d
0	0.296609	-0.038840	0.004960	0.000000
1	0.068320	0.017870	-0.019190	0.000000
2	0.002869	0.006220	0.000000	0.000000
3	0.000240	-0.002090	0.000000	0.000000

Table 1.3: Rydberg-Ritz coefficients for triplet helium atoms. Calculations from Prof. Thomas Bergeman. Figure from Xiaoxu Lu's thesis [11].

Electrons with smaller angular momentum tend to have a higher quantum defect as their orbits are more likely to penetrate the shielding electrons as we can see in the table. On the other hand, states with higher l values will have lower quantum defect effects as the quantum defect of $l = 3$ is three orders less than that of the $l = 0$ states as their orbits stay distant from the core.

1.2.4 Stark Effects in Rydberg Atoms

The large separation between the atomic core and the outer electrons of a Rydberg atom gives it a very large electric dipole moment d. For a hydrogen atom, the interaction between the atom and external field can be expressed as [21]

$$(-\frac{1}{2}\nabla^2 - \frac{1}{r} + Fz)\Psi(r) = W\Psi(r) \tag{1.6}$$

where F is the applied electric field in atomic units (5×10^{11}V/m) and this equation can be solved analytically because the terms can be separated using parabolic coordinates. Whereas for non-hydrogen atoms, the situation is different. The terms can not be separated and we could not solve it analytically. However, it is still possible to numerically estimate the elements of the resulting matrix [21] which is described by Zimmerman et al..

Figure 1.1 is a Stark effect simulation of $n = 26$ state for helium atoms. From the figure we can extract some useful information: 1) Due to quantum defects there is a strong depression of the S, P, states; 2) The degeneracy of the $l > 3$ state is lifted at zero field; 3) As the electric field intensities rise,

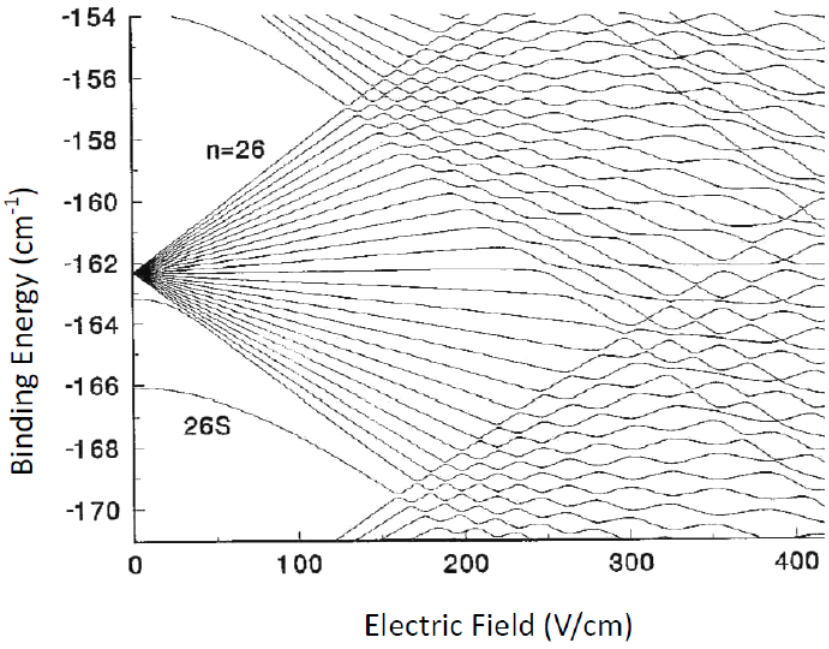

Figure 1.1: Stark map for a helium atom at $n = 26$ state made by Prof. Thomas Bergeman [12].

avoid crossings emerge because the ionic core for non-hydrogen atom breaks the Coulomb symmetry and couples the Stark levels with each other.

When there is an external field applied, quantum number l does not describe the states well any more. Because l values for different states are mixed on the map and the only state that can be distinguished, as we see from figure 1.1, is 24S state and only at low field intensity, and the mixed l states are known as the *manifold* part in the Stark map. We will use this notion very frequently in the rest of this thesis.

We can calculate the oscillator strength of different states so we can look into the transitions. The oscillator strength from level $|nlm\rangle$ to $|n'l'm'\rangle$ is

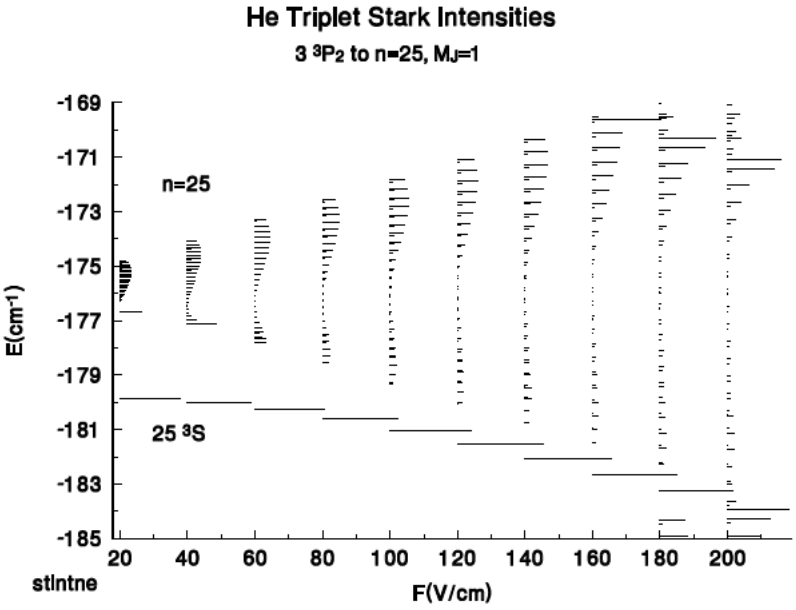

Figure 1.2: Transition strengths from $3^3\mathrm{P}_2$ of $n = 25$ states triplet helium atoms [12].

$$f_{nlm,n'l'm'} = 2\frac{m}{\hbar}\omega_{n'l',nl}|\langle n'l'm'|z|nlm\rangle|^2 \tag{1.7}$$

The oscillator strength of helium atoms can only be evaluated by numerical integration. The resulting transition intensities of the $n = 25$ states are from the previous thesis of Yuan Sun [12] where the data is provided by Prof. Thomas Bergeman as is shown in figure 1.2.

We can see when the electric field intensity increases, the strengths of the manifold states begin to split, and the other n states would behave similarly. These different oscillator strengths can lead to different Rabi frequencies as we are about to mention. To excite atoms to the different states in the manifold

on the Stark map, we have to produce light with the corresponding frequencies.

1.3 Helium Excitation to Rydberg States

In our experiment, the goal is to produce helium Rydberg atoms and to maximize the transfer efficiency. Since there is one more electron in helium atom than hydrogen atom, things are quite different. The two electrons can have parallel spins (triplet) or opposite spins (singlet), so the total spin could be 1 or 0.

As in figure 1.3 below, because of the selection rules we can not use optical methods to directly excite the ground state helium atoms to the metastable state 2^3S_1 state and the metastable atoms can not decay to the ground state either. This will give the metastable state (created from a electric discharge) with energy of 19.8 eV a very long life time and that is the reason why we choose this state to be the starting state in the STIRAP experiment. The 1083 nm laser that connects the 2^3S_1 state and the 2^3P_2 state is for separating the Rydberg atoms and the metastable atoms and does not participate in the 2-step excitation process.

As we see in figure 1.3, the transition we want to make is from the 2^3S_1 state to the 3^3P_2 state using a coherent light field. There is a three level ladder system above the metastable state, and the Rydberg states lie on the highest one. A second laser with ~ 790 nm wavelength further excites the intermediate state to the Rydberg states. Both the lasers come from independent Ti:Sapphire laser

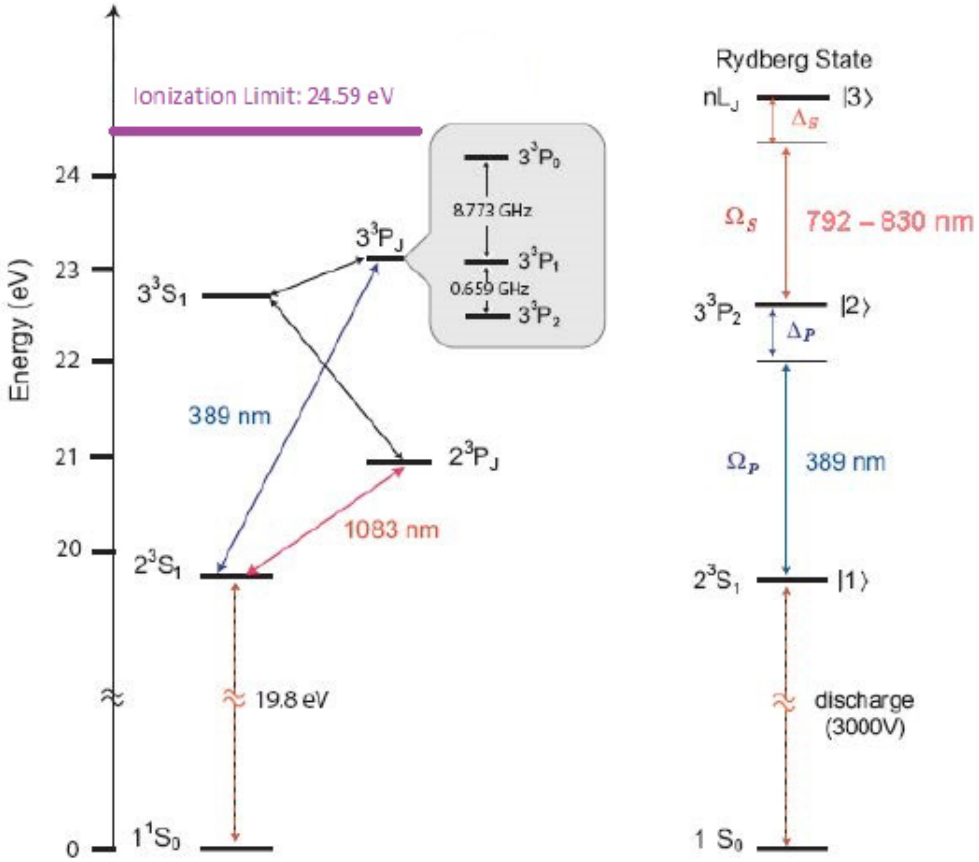

Figure 1.3: Energy levels with corresponding wavelength lights and the 3-step transition [11].

systems in our lab, and we may scan the electric field or the red laser frequency to excite the atoms to different Rydberg states as the 389 nm laser that connects the metastable state and the intermediate state is always kept locked to make the transition.

The Rydberg atoms are easy to ionize and we may use an ion detector to detect the Rydberg atoms created in our system. It can also be picked up using the SSD detector in the system.

In this thesis, Chapter 2 and Chapter 3 are about the apparatus in the STIRAP experiment. Chapter 2 introduces the vacuum system environment for the helium excitation as well as the detectors for data collection. Chapter 3 discusses the three laser systems to produce the lasers for our transition and measurements.

In Chapter 4, we introduce the STIRAP technique for maximizing the transition efficiency. It is also based on a three state ladder system of the helium atoms only with counter intuitive laser beams timing to maximize the efficiency. Theoretically the STIRAP efficiency could get as high as 100%.

Chapter 5 and Chapter 6 are mainly about the measurement and data analysis, including the absolute STIRAP efficiency and the Rydberg atom signal. Since we have not yet successfully obtained Rydberg atoms data, data and results from previous theses are being used here. Credits are given to the authors: Seung-Hyun Lee, Xiaoxu Lu, and Yuan Sun [10] [11] [12]. Here I humbly express my gratitude to them and my advisor Professor Doctor Harold Metcalf.

Chapter 2

Vacuum System

2.1 Introduction

The vacuum system we are using in the STIRAP experiment, as sketched in figure 2.1 [12], contains three main parts: the Source Chamber, the Interaction Chamber, and the Detection Chamber. Metastable helium is created in the Source Chamber; The STIRAP process happens in the Interaction Chamber; And the detection signal is picked up in the Detection Chamber. The whole system is made mostly by stainless steel and conflat flanges sealed with copper gaskets.

We always need to maintain low pressure in all three chambers to keep the atoms traveling straightly. The Source Chamber and the Interaction Chamber are separated by a wall so they can be differentially pumped. Only a small aperture allows helium from the source to pass for our experimental use. The

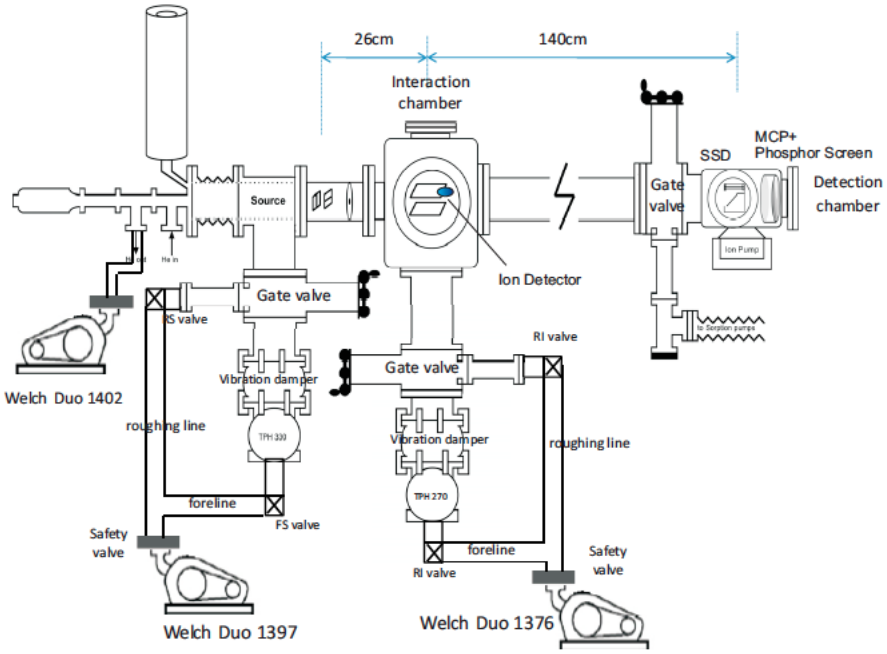

Figure 2.1: A brief scheme of the vacuum system. As introduced the whole system contains three major chambers [11]. Usually the pressure in the chambers needs to be kept as low as $\sim 10^{-6}$ Torr.

Source Chamber is pumped by a Pfeiffer TPH 330 turbo pump backed by a Welch mechanical pump model 1397. The Interaction Chamber is pumped by a Pfeiffer TPH 270 turbo pump backed by a Welch mechanical pump model 1376. An extra Welch mechanical pump model 1402 is used to pump out the back flow of the helium gas from the Source Chamber to maintain a steady pressure in the chambers. Though the Detection Chamber and the Interaction Chamber are connected with each other, there is a long beam line between them so we need to pump the Detection Chamber independently. An ion pump is set there to keep the pressure low enough.

Several pressure gauges are deployed so we can monitor the pressure at different places at different times. A digital display Granville-Phillips pressure gauge monitors the pressure in the foreline region before Source Chamber, and we should always see a sharp rise of pressure once we open the valve and let helium flow into the stream lines during the purging phase which will be mentioned in the following section (usually when there is no helium flow the reading is around 400 mTorr and once the helium flows in, it rises to several Torr and slowly goes down as the gas is being drained out by the mechanical pump). Four Granville-Phillips gauges are used to monitor the pressure in and before the Source and Interaction Chamber: SF, SR, IF, IR. Though the scales of these gauges are not fine enough to monitor the real pressure of the chambers which could be down to 10^{-7} Torr, the readings can be a good reference to tell if the system is working normally and if we are ready to introduce turbo pumps. The pressure readings should be: IF 2×10^{-2} Torr, IR 0.5×10^{-2} Torr, SF 1.5×10^{-2}

Torr, SR 0.8×10^{-2} Torr when everything works normally, and when the helium flows in, all the readings should go up a little bit. Two ion gauges with degasing systems monitor the real pressures in the chambers. The readings are on a level of 10^{-7} Torr without the source running and a level of 10^{-6} with the source running.

The vacuum system is designed so that the chambers can be vented to the atmosphere with the turbo pumps running. Two gate valves G1 and G2 sealed by 6 inch O-rings are set between the turbo pumps and the chambers to guarantee that the chambers are well sealed once they are closed. There is also a gate valve between the Interaction Chamber and the Detection Chamber that can be shut if needed. When we need to vent the system to the atmosphere under circumstances like we need to replace the pieces in the chambers or the system is not being run for several days, what we usually do is we close the gates between the turbo pumps and the chambers and the gate of the Detection Chamber and open the foreline valves IF and SF (valves between mechanical pumps and the chambers) to let the mechanical pumps directly pump the chambers, then we shut down the mechanical pumps if necessary. When we need to turn the system back on, turn on the mechanical pumps first and wait for the pressure go down to the level of 100 mTorr which is the best the mechanical pumps can do. Then we open the connection valve between the Welch mechanical pumps and turbo pumps to back the turbo pumps on and shut valves IF and SF. Open the gates G1 and G2 so the chambers with pressure already down to 100 mTorr can be directly pumped by the turbo pumps. As for the Detection Chamber, things

are easy. Just sealing the gate valves and turning off the ion pump will do the job.

To prevent the pump oil from back streaming under a power outage, safety valves are placed on the mechanical pumps that can immediately shut themselves when the pressure in the chamber is lower than the mechanical pump side. This way the oil contamination can be minimized.

2.2 Source Chamber

We already made it clear that there can not be any transition between the 2^3S_1 state and the ground state because it is doubly forbidden by the selection rules. So optical transition do not create the metastable helium atoms in this case but an electric field generated by a DC discharge. We refer this discharge as the source below. It was first designed by Kawanaka et al. [22] and slightly modified by Mastwijk et al. [23]. Our source is built at Utrecht University. This process usually excites a portion of 10^{-5} of the total helium atoms to the metastable state, not a large number but certainly enough for our STIRAP use.

As shown in figure 2.2 [24], the source is composed of a glass tube and a skimmer plate. The glass tube is tightly fixed on to the skimmer by a rubber O-ring on the narrow and and a Teflon layer on the other end in the stainless steel chamber which is cooled by liquid nitrogen to ~ 70 K. This whole chamber is sealed and it only allows the helium to flow in and out via the stream line. Our Teflon sealer is a bad electric conductor and a good thermal conductor

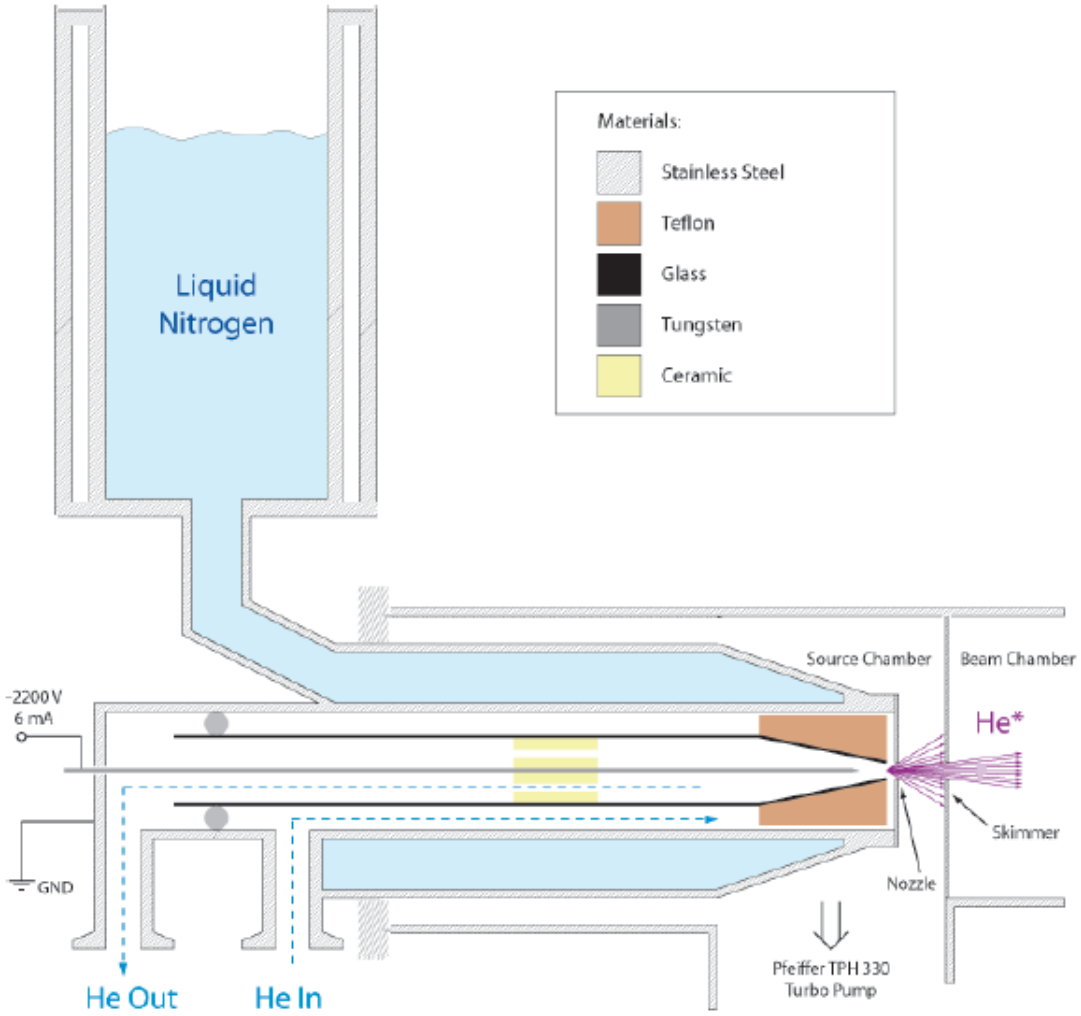

Figure 2.2: Source Chamber structure. Figure from Yuan Sun's thesis [12].

thus the atoms at the end of the tube would be effectively cooled and the discharge is kept stable. As in 2.2, there is a tungsten needle serving as the cathode of the DC discharge with a voltage of ∼-2200 V provided by a voltage-controllable DC power supply. This needle is held by ceramic spacers (which are

also insulators) in the middle of the glass tube. This discharge ionizes the helium atoms that then recombine into the metastable states and the metastable atoms will then flow past the nozzle plate attached on the glass tube which serves as the anode. After that there is a skimmer plate with a 3 mm aperture on it. This plate separates the Source Chamber and the Interaction Chamber. Helium that flows through the aperture enters the Interaction Chamber and takes part in the STIRAP process. The aperture also limits the helium flow and forms the atomic beam we are using. It is not only the metastable helium that flies pass the aperture, but along with the ground state helium left, charged particles, UV and visible light.

To guarantee a steady and reliable source power, certain parameters have to be taken caution of. In regular experiments, the pressure in the source chamber should be less than 4 Torr with helium running, controlled by the needle valve in the stream line. Higher pressure could lead to less metastable helium, the probable reason is with higher flowing speed, the discharge becomes unstable, causing fewer atoms to be ionized. Low pressure would also cause fewer metastable atoms because the total number of atoms passing through the source region is lower. Experimental results show that the best pressure with helium running should be around 2.2 Torr [11], and to keep the pressure in the wanted range, we need to always make the nozzle clean and not blocked which will lead to a pressure build-up in the chamber that prevents source from being lit. The voltage between the tungsten needle and the nozzle is usually kept at $\sim$ 2200 V. The current is also a decisive parameter of the source, and in this

experiment, it is usually $\sim$ 8 mA. What is to be noted is that the higher the current is, the faster the helium flow is. This way running the source with high currents significantly shortens the lifetime of the source. So we add a 100 MΩ resistor in the circuit to limit the current and run the source in a current limiting mode. When the resistor is burnt and the current goes beyond the limit, the source will not light, either. The details are in the adjustment section.

In practice, the procedure to turn on the source takes a few more steps than we thought. First we have to purge the system to get rid of the gas in the tubes before the system. The tubes are made of plastic so it is easy for the gas molecules to get in. Close the drain valve that is between the forelines and the mechanical pump. This way the connection is shut and what was in the pipes is isolated. Then open the helium tank, wait for a few seconds, and close it to let gas flow in and the pressure in the pipes to build up. Open the drain valve again to let the gas being pumped out. During this process we could see the pressure in the forelines goes up to a fairly high level (usually several Torr) first and then slowly goes down. It is simple to understand this step: Let the helium flow in and then get pumped out of the forelines, this process flushes out what was left in the pipes before the experiment. During everyday experiments we do this four times to ensure there will not be any irrelevant gas in the system.

Once we are ready to let gas flow in the Source Chamber, we open the valves labeled Whitey (the flow valve) which is the manufacturer name and valve V1 (the back flow valve). The flow valve controls the Source Chamber flow and V1 is between the mechanical pump and Source Chamber forelines. When V1 is

open, mechanical pumps are beginning to pump out the back flow of the helium gas to ensure a steady pressure in the chamber.

It usually takes a few minutes for the helium flow to stabilize. Further more time is needed for the liquid nitrogen to cool the whole chamber and lower the pressure. With helium flowing in and the pump that controls back flow is on, we pour in liquid nitrogen and wait for the pressure to drop. The readings on the Granville-Phillips gauges that indicate the pressure in the chambers will tell us that (the pressure in the Interaction Chamber will drop little because the Interaction Chamber is further away from the nitrogen tank and it is a lot bigger so its harder for the pressure to drop significantly). Another sign that marks we are ready to proceed is the nitrogen tank. When we first add liquid nitrogen to the tank, it will fast vaporize under room temperature so the liquid surface is highly unstable and we can see with naked eyes that air bubbles emerge fiercely on the surface. We keep adding liquid nitrogen as it evaporates into gas form. When the liquid surface is on a steady level and relatively stationary, the system temperature is down to a low enough level for the nitrogen to stay in the liquid form. Here we can carry on to the next step. We can also see that a frost layer formed by the water in the air is built around the nitrogen container at this point.

As the equipment aged, by the end of 2014 we needed higher voltage to keep the source running normally, which is ~ 2300 V. When the source is lit we can see it is glowing gentle blue when it is working normally, emitting metastable helium plasma. During the experiment the source dies a lot (the source stops

glowing and there is no current as we can read on the front panel of the control box of the source) and we need to restart the source. The reason leads to that could be the pressure is too high or the source voltage is lower than the threshold.

Sometimes the source will simply not light when we turn on the voltage even with appropriate pressure. Adjusting the needle position and raising voltage may fix that. There is a conflat window on the Source Chamber so that we could observe the source light plasma. As is introduced above, a light blueish glow is expected. Occasionally there is a yellow spot instead of glowing blue in the discharge region, this is probably there is a discharge staying in the glass tube not coming out through the nozzle. Usually this happens due to the pressure inside the glass tube is too low and the atoms are less likely to fly out of the tube. We may open the flow valve, let more helium in to increase the interior pressure to push the metastable atoms out and solve that problem. Once the source starts to light again, we need to reduce the pressure back to the normal level to make sure the source run steadily (the source could not run for a long time under high pressure). Sometimes the blue is a lot dimmer than we expect, this just indicates that it is not the right discharge state.

We can always monitor the efficiency based on readings from the detectors that we are about to introduce. Sometimes even when the source is working, there may not be metastable atoms going in to the Interaction Chamber. This could be the misalignment of skimmer position. So the source induced plasma can not pass through the aperture and move into the interaction region. Or the

nozzle is not clean so the atoms passing can not form the beam as we want, it can be scattered or deflected.

In all, the current, the pressure in the chamber, the nozzle and needle parameters could all affect the production of source beam. To maintain the function of the source, these should all be taken care of.

2.2.1 Time of Flight Measurement

In our experiment, a necessary parameter is the longitudinal velocity of the atomic beam. Since not all atoms in the beam are traveling at the same velocity, we need to know the longitudinal velocity distribution. It is obtained through a time of flight measurement. We use a chopper placed inside the vacuum system and the SSD detector in the detection chamber. The distance between the detector and the chopper is 1.4 m. We already mentioned that not only the atoms fly out through the skimmer, but also photons. This way by measuring the arrival time of the photons and the atoms, we can obtain the longitudinal velocity profile of the atomic beam. The chopper moves at a resonant frequency with a small slit on it, allowing atoms and photons passing through. Figure 2.3 is a typical signal reading of the time of flight measurement profile. The chopper periodically moves and blocks the beam, creating standing peaks in one cycle. The front peak indicates UV photon signal from the source, and the second peak is from the metastable atoms. The reason that there is a spread of the photon peak is that the chopper can not move as fast as the photons. We can see the time delay between the two peaks is roughly 1.25 ms. Considering the speed of

light is so high and the time for the photons to travel 1.4 meters is so small, we can basically treat this 1.25 ms as the time of flight for the atoms to reach at the detector, and this gives an average longitudinal velocity of 1070 m/s and a spread of ±240 m/s in a shape of Gaussian (data from Xiaoxu Lu measured in 2007). It is not negligible that there is a not-so-small longitudinal velocity spread of the atomic beam. The measurement is done with a flow pressure of 1.8 Torr and needle voltage of $\sim$ 2.3 kV and current of $\sim$ 8 mA.

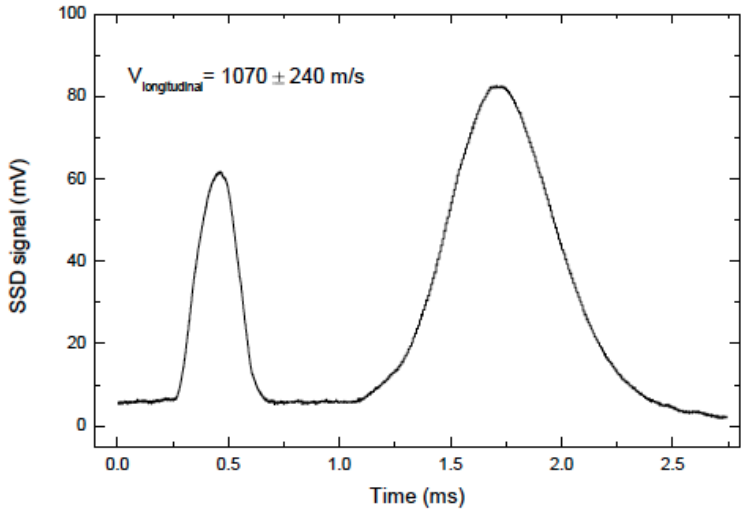

Figure 2.3: Time of Flight measurement [11]. The data comes from Xiaoxu Lu's thesis. The second peak indicates the traveling speed of the atom and the velocity spread.

2.3 Interaction Chamber

About 26 cm downstream from the Source Chamber (the skimmer) in the system is the Interaction Chamber. The major elements in this chamber are

two field plates, an ion detector and a electro-static lens which focuses the beam going into the detection region.

There are two slits, one horizontal and one vertical, before the field plates in the chamber, which can be used to adjust the beam position (monitored by the phosphor detector that we will talk about later).

On both sides of the steel chamber, there are conflat windows that are non-reflective to the certain wavelength beams we use mounted on 6-inch flanges for the laser beams to go in and for us to observe, not the STIRAP process itself for it can not be seen, but rather the installations inside. Like if the ion detector is on the right position, or if the beams are hitting the right position. There are four flanges of BNC feedthrough connection ports for us to feed and control voltages of the equipment.

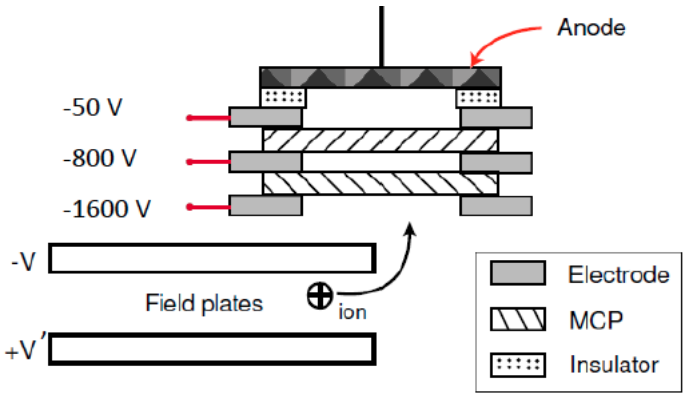

Figure 2.4: Interaction chamber and ion detector [11]. The ion detector collects ions generated from Rydberg atoms to detect their existence.

As we can see in figure 4, the STIRAP happens here. The atomic beam and the laser beams coming in through the window cross in the middle of the field

plates, creating Rydberg atoms. At a few centimeters downstream, the atomic beam meets the 1083 nm laser which only acts on the remaining metastable atoms, and the field plates themselves provide an adjustable sweeping electric field in the experiment. There are roughly thirty small holes with the diameter of several millimeter forming an array on the top plate to allow the ionized Rydberg atoms to fly through and get picked up by the ion detector. The ion detector sits right above the array or is moved to a position several centimeter downstream of the field plates depending on our need. Due to the maintenance requirements of the vacuum system, the ion detector on the plate is not fixed. It actually rather stands on the top plate. This creates a lot of trouble for us during the process of opening the chamber and fixing the equipment and connections. There are four resistors on the plates that are used to produce the heat needed for blackbody radiation, which we will talk about later.

2.3.1 Ion Detector

The most important part in the Interaction Chamber is the ion detector, which sits on the top plate and a little bit downstream of the lasers. As in figure 2.4, the ion detector consists of two MCPs (micro channel plates), three electrodes with voltage of ~ -2000 V, ~ -1000 V and ~ -20 V and an anode to collect the signal all held together by three plastic rods.

The microchannel plates play a crucial role in the ion detector as well as the other two detectors. A microchannel plate is a slab made of highly resistive material that will emit electron once hit by an ion or an electron. This property

allows it to act as an array of continuous electron multipliers under strong electric fields. The plate itself is 2 mm thick. The reason it is named microchannel is that there are thousands of small channels fused on the plate. The channels form an array on the plates leading from one side to the other. Each channel is approximately ten micrometer in diameter (six micrometer for high resolution ones) and separated from each other by a distance of average 15 μm. The channels are all deployed at an angle with the surface and parallel with each other so that the particles entering the channels are guaranteed to hit the wall either on the plane of the plate or the channel wall, and this process will free electrons from the wall and produce an electron-accelerating potential difference across the channel thus increase the potential. The electron will then hit the next wall and free more electrons via secondary emissions. This process will repeat as the electrons are being accelerated along the channel. They will hit the walls again, till then they move out of the plate from the other side, creating much stronger signal than the incident particles. Thus the original signal is amplified by several orders of magnitude.

The MCPs we use were purchased from Burle Electro Optics. The channel diameters are ten microns with a spacing from one center to another of 12 microns. The impact angle is 12°, with a length to diameter ratio 40:1, and the gain is $\sim 10^3$ at 750 V bias voltage and $\sim 2 \times 10^3$ at 800 V. The gain will slowly change as the plate itself ages.

There are two MCPs in our ion detector. The channels of them are rotated into the opposite direction, forming a V-shape arrangement. The three

electrodes with high negative voltage will attract the blackbody induced ions. Then through two consecutive signal amplifications, the anode on top will pick the electron signals and send it to a voltage-current converter and then to an oscilloscope and read by us.

2.4 Detection Chamber

The last major part of our vacuum system is the Detection Chamber. It contains two detectors and is pumped separately by an ion pump. The phosphor screen detector provides a spatial image of the transverse beam profile. The SSD detector is used to measure the absolute efficiency of the STIRAP process. That is, the Rydberg atoms count versus the residual metastable atoms count.

2.4.1 Phosphor Screen Detector

The Phosphor Screen Detector (PSD) provides us an image of the spatial distribution of the atomic beam, converting the initial radiation into a glowing image. It is used to show us the beam position, for alignment and observation of the momentum transfer ("the push"). We can monitor the beam image as we move the slit position to maximize the beam brightness and adjust the beam position. However, it will not give us quantitative measurement results. The basic map of the PSD is shown below in figure 2.5. There is also an MCP in the detector, receiving incoming atoms and amplifying the signal. Our metastable atoms, due to their high internal energy, can also cause secondary emissions of the MCP plate. This process does not distinguish the Rydberg atoms and the

metastable atoms thus it can not be used to take any experimental data. The electrons emitted by the MCP will then fly towards to the phosphor screen, and finally, the phosphor screen will emit visible light which can be observed with naked eyes or a CCD camera which is deployed several centimeters out of the window of the Detection Chamber.

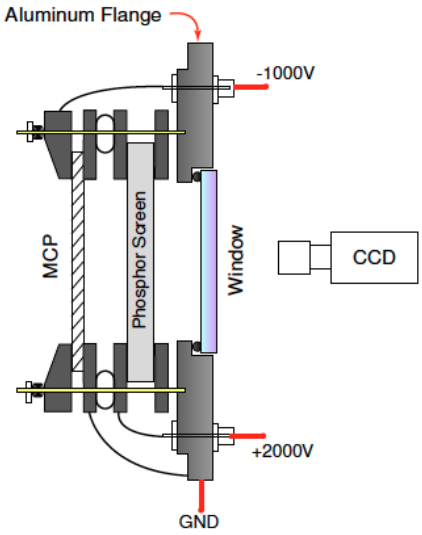

Figure 2.5: Phospher Screen Detector [10]. We can acquire the spatial information either through naked eyes observation or CCD camera.

Our phosphor screen is bought from Lexel Imaging System, made of glass and Indium Tin Oxide (ITO) and P43 phosphor. The light emitted from the screen is from the P43 covered on the screen and peaks around 545 nm. That is, from yellow to green. But since not only atoms but also photons will take part in the imaging process so the light intensity will not be proportional of the incoming atoms number. So it can not be the measurement reference of quantitative atomic beam profile. Still it is really convenient for a straight

observation. If we further want a good quantitative measurement, we have to refer to the SSD detector data.

2.4.2 Stainless Steel Detector

We already mentioned that the time of flight measurement is done through the SSD, measuring the arrival time of UV photons and atoms to the detector. Figure 2.6 shows a brief scheme of the SSD. The output of the SSD is proportional to the incident numbers of the metastable helium atoms so it provides good quantitative measurements.

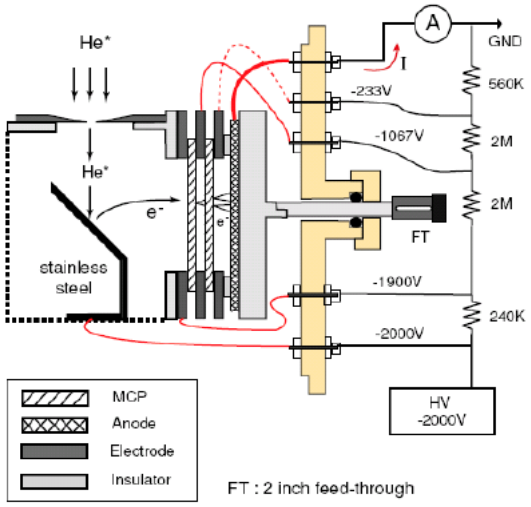

Figure 2.6: Stainless steel detector [10].

The mechanism of the SSD is fairly simple: Incident atoms hit the stainless steel and emit electrons which will then fly towards the MCPs and create second emissions. The signal from second emission is then picked up by external circuits and then fed in to the oscilloscope. Our SSD is mounted on a Huntington

Mechanical Laboratories, Inc. 2-inch linear motion feedthrough so it can be moved to measure different position in the chamber.

The SSD detector detects signals generated by both metastable atoms and Rydberg atoms. To transversely separate them, we need the 1083 nm laser beam which we will introduce in the next chapter.

Chapter 3

Laser Systems in the Experiment

We are using three different laser systems for the STIRAP experiment: The 389 nm laser which we will refer to as "the blue" laser that connects the metastable state $|1\rangle$ (2^3S_1) and intermediate state $|2\rangle$ (3^3P_2), the $\sim$ 796 nm laser that connects middle state $|2\rangle$ and the Rydberg states and we call it "the red laser". We are sweeping this red laser or the electric field generated by the field plates in the vacuum system to scan through the Stark manifolds. Both the blue and red laser are produced by two independent Ti:Sapphire lasers (Ti:Sapph). The 1083 nm laser drives the $|1\rangle$ state to the 2^3P state and gives it a momentum and "pushes" it away to separate it from the Rydberg atoms for the SSD detection. This laser is not involved in the STIRAP excitation process

and is solely devoted to the measurement process.

3.1 389 nm Laser System

3.1.1 Introduction

The blue light scheme is shown in figure 3.1. The 389 nm blue light comes from the output of an SEO (Schwartz Electro-Optics) Ti:Sapphire laser after a frequency doubling process. The SEO Ti:Sapph is pumped by a Sprout-G laser produced by Lighthouse Photonics. With a 10 W multi-wavelength pumping light going into the Ti:Sapph, it generates infrared light with wavelength of 778 nm at around 2 W [11], set in a ring configuration to avoid the spatial hole burning effect. A frequency doubling unit (Coherent Model MBD 200) doubles the frequency of the light coming out of the SEO Ti:Sapph through the second harmonic generation process (SHG) and turns it in to the 389 nm blue pump laser we need in the STIRAP process. Different locking systems are deployed onto the laser systems to lock the frequency and protect it from temperature change, small vibrations and other fluctuations that may cause the lasers to be off-resonance. There are three locking mechanisms in this blue laser system: A Pound-Drever-Hall (PDH) lock is used to stabilize the Ti:Sapph and lock the frequency to a Fabry-Perot cavity; A Hänsch-Couillaud (H-C) technique that locks the light coming out the MBD doubling cavity; A Saturation Absorption Spectroscopy (SAS) system locks the Fabry-Perot cavity against environmental noises and the feedback is further sent back to the PDH system.

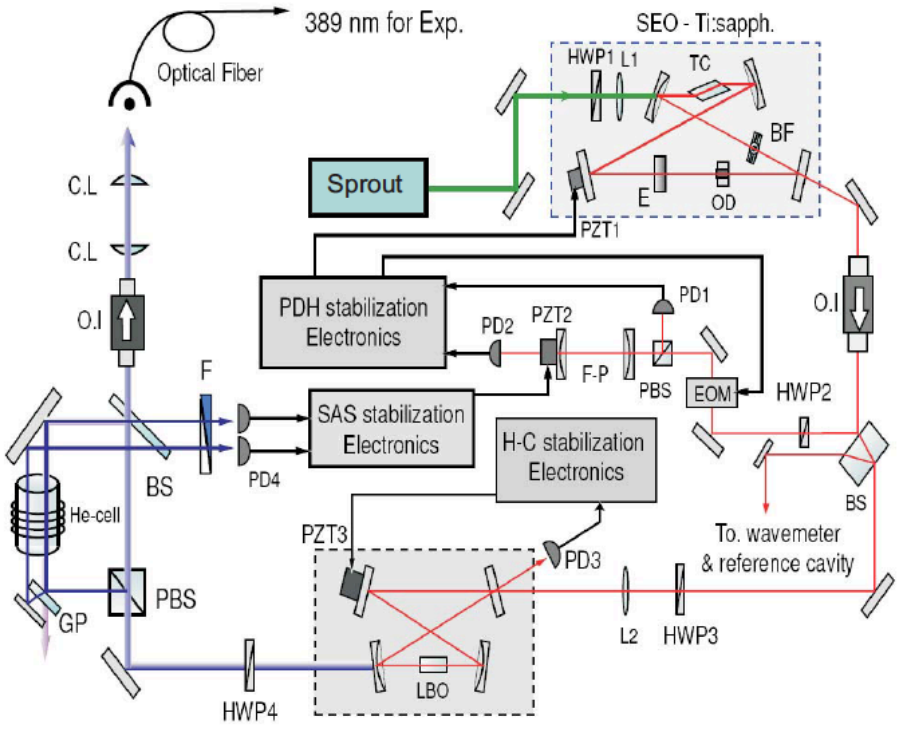

Figure 3.1: Blue laser scheme [12]. Three frequency locking systems are deployed to generate the 389 nm laser.

3.1.2 SEO Ti:Sapphire Laser

The SEO Ti:Sapph is running in a ring mode (the path of the laser forms a closed loop so there will not be counter propagating lasers overlapping with each other which will lead to the spatial hole burning effect) to produce CW light. In the Ti:Sapph laser system, a sapphire crystal doped with titanium ions acts as the gain medium. Four mirrors-two flat and two curved-form a lasing cavity. There are five more optics added in the system as is in figure 3.1 for different uses. A half wave plate before the cavity guarantees the light polarization matches the polarization direction of the crystal. A focusing lens L1 focuses the pumping light going in to the crystal and narrows the beam width. Along the path in the cavity there are two mode selection tools: An etalon and a birefringent filter for us to control the wavelength. A 778 nm wavelength is the goal for our alignment of the SEO Ti:Sapph. Furthermore there is an optical diode to ensure the light travels in the right direction and to prevent interference with the reflection of its own from the mirrors. When we need to optimize the power of the laser, that is, adjusting the cavity length. We usually adjust the PZT mirror and the output mirror in the cavity. When the laser is aligned well, we should have a power around 2 W with a 10 W pumping power from the Sprout-G laser.

The laser coming out of Ti:Sapph will go straight through a Faraday isolator and a beam splitter. Then it gets divided into three parts and will be used for MBD doubling for the final output; The PDH locking that stabilizes the laser modes of the Ti:Sapph; Wavemeter that monitors the wavelength of the laser

coming out.

The alignments of the SEO Ti:Sapph is similar to and rather simpler than the red laser system Tekhoscan Ti:Sapph so the alignment process section will be under the 796 nm laser system introduction.

3.1.3 MBD Frequency Doubling and the Hänsch-Couillaud Locking

Our lab uses a Coherent MBD-200 frequency doubling unit. A Lithium Triborate (LBO) crystal which is a non-linear crystal plays the main role in the frequency doubling process. It is pretty close to a normal crystal laser system except the gain medium is a non-linear crystal. This is done through second harmonic generation (SHG) by letting the 778 nm laser light pass the non-linear crystal. Then we get light output with doubled frequency at 389 nm. The output window glass is designed to be highly transmitting for 389 nm laser but highly reflective for 778 nm laser.

As is in figure 3.2 [10], the laser from SEO Ti:Sapph goes in to the unit after passing a half wave plate and a mode matching lens. The half wave plate sets the polarization direction of the incoming laser and forms a small angle between it and the crystal axis. The reason for this will be mentioned in the following section. We can access the two steering mirrors and adjust them to align the laser and maximize the beam power going in because they have adjusting mounts on the outside of the box.

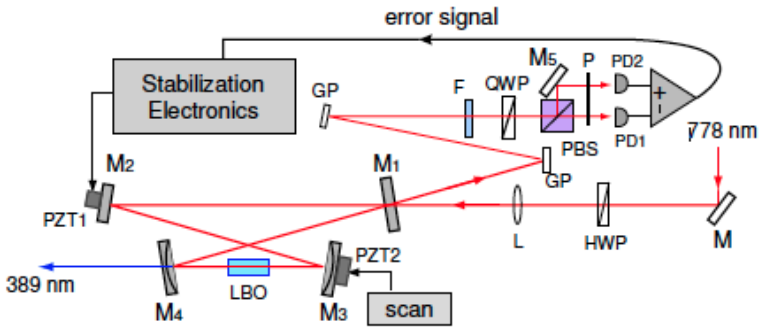

Figure 3.2: MBD doubling system with H-C lock [10].

Second hamonic generation The non-linear properties allow the crystal to generate second harmonic light, and the total power being generated through one single pass is [25]

$$P_{2\omega} = \gamma_{SHG} {P^2}_{\omega} \tag{3.1}$$

where P_ω is the fundamental power of the laser and γ_{SHG} is the second harmonic generation coefficient which depends on the crystal properties [26].

External SHG cavity Letting light pass the crystal once does not generate enough power outcome as in equation 3.1, the γ_{SHG} is set when we chose the LBO crystal and the gain is not enough in our case. Apparently there are limitations of the fundamental power P_ω. To get high enough second harmonic power for the STIRAP experiment, we need an enhancement cavity to make the beam go into the crystal multiple times and further stabilized on resonance. For a given fundamental power P_ω, the total power after the resonant cavity

enhancement P is

$$P = \frac{P_\omega T_1}{(1 - \sqrt{R_1 R_m})^2} \tag{3.2}$$

The R_1 and T_1 above are the reflection coefficient and transmission coefficient of the input mirror. R_m is the loss all over the rest of the mirrors in the round trip in the cavity, including loss on crystal dispersion, reflection on the rest mirrors, etc. We know that $T_1 + R_1 = 1$ and from this we can see that when R_1 equals R_m the maximum circuit power is achieved. That's the basic selection and building rules of the SHG cavity. Installation of the MBD unit and the enhancement cavity is similar to what we will get to in the red laser section. We can look inside the doubling cavity, there are four cavity mirrors forming a ring configuration similar to the SEO lasing cavity. The following procedures to align it are on a basis of following the light path. We first adjust the steering mirrors to make sure it hits the middle of the input coupler and the PZT mirror M2. Adjust M2 to make the beam hit the spherical mirror M3. Then adjust the knobs on M3 to make the beam pass the center of the crystal and hit the same spot where the incoming beam hit on the input coupler. This way we form a closed loop for ring configuration. We can monitor the output at double frequency coming out and adjust the mirrors to maximize the power output. So far the best power out of the MBD is ~ 300 mW.

Since some knobs and optics can get loose and change positions due to weather changes or temperature perturbation, causing the resonance cavity length to change. This requires a feedback signal onto the cavity to keep the frequency locked. So we introduce feedback locking systems to stabilize the

lasers.

Hänsch-Couillaud locking system The method we use to lock the frequency doubling system on resonance is known as "Hänsch-Couillaud method" [27]. It measures the the polarization of light reflecting back from the input mirror in the cavity. The principle of all laser feedback locking systems is all about acquiring the error signal: The information of how far and in which direction the laser is off resonance. We can compare the laser with a reference which stays at the resonance frequency we want to "tie the laser with" and get this information. For the H-C method, we know in the frequency doubling cavity only the light component with the same polarization direction of the crystal optical axis will get frequency doubled and pass the cavity [28]. The cavity is designed so that any incoming light component with the perpendicular polarization direction will be simply reflected back by the input coupler M1. In our locking system, the laser goes through a half wave plate whose polarization direction forms an angle of θ with the crystal transmission axis before going in to the cavity. This way the vertical component signal bounced back from the input coupler can serve as the reference. The parallel component goes in and, if the cavity length is slightly different from the laser resonance length, experiences a frequency dependent phase shift and is reflected by the output mirror (the standard 389 nm light will simply pass the cavity) and comes out through the input coupler M1. This is the phase difference information we want to extract and use for the error signal. Now the laser coming out from the input coupler M1 is

picked, it should contain two components: Vertically polarized light reflected by M1 and horizontally polarized light passing the crystal and being reflected by the output mirror with a phase difference. Note that if the cavity is on resonance there should not be a parallel polarized component coming out as the output mirror is highly transmitting at the wavelength of 389 nm. Thus what comes out now should be a linearly polarized beam, and further circularly polarized after going through the quarter wave plate out of the cavity. But if the cavity is off resonance, the phase of the horizontal component should be slightly ahead or behind the vertically polarized light reflected by the input mirror depending on the cavity length is longer or shorter, making an elliptically polarized beam come out. Then, after the light passes a polarization beam splitter, two photo diodes are used to measure the relative intensity difference of the split beams with horizontal and vertical polarization. A polarization sensitive analyzer is used to extract the cavity length information. If the cavity is on resonance there should be no difference between the two signals, but if there is a difference, it indicates the cavity is off resonance. The measured difference signal is:

$$I_1 - I_2 = 2I \cos\theta \sin\theta \frac{T_1 R_m \sin\delta}{(1-R_m)^2 + 4R_m \sin\frac{\delta}{2}} \tag{3.3}$$

where I is the intensity of the incoming beam and I_1 and I_2 are the two intensities measured by the photo diodes. This serves as the error signal of the feedback system, and the sign of this intensity reading indicates the off resonance direction of the laser. Typical signal is presented below (data from Xiaoxu

Lu in 2011).

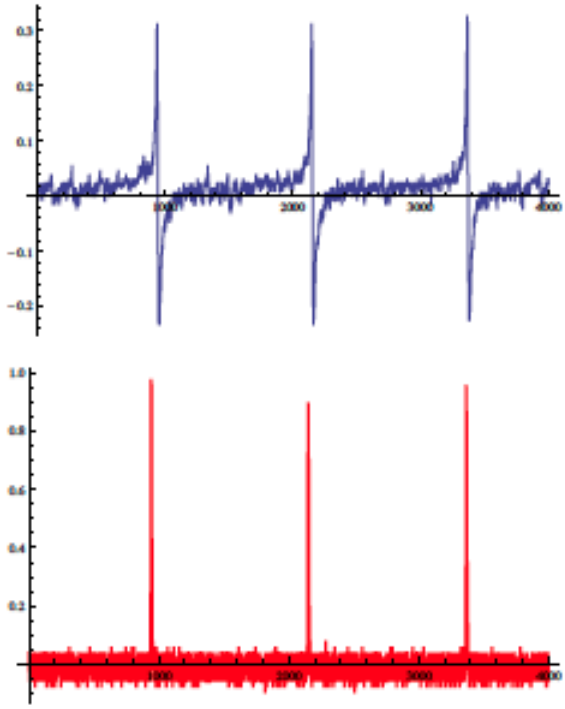

Figure 3.3: Top: Error signal of the H-C locking system; Bottom: Power monitor signal [11].

We see in the first graph of error signal, as the laser frequency is being scanned, the error signal appears to be several anti-symmetric peaks. The slopes between the peaks are exactly at the same positions with the signal peaks in the graph below. These peaks in the upper graph indicate where the maximum feedback signal is needed, and the sign means the laser off resonance direction. As we see in scan mode when the laser is on resonance, the feedback signal is zero and the power output is maximized as there are peaks in the lower graph

now. We can optimize the error signal by adjusting the half wave plate and the quarter wave plate (the quarter wave plate is in the MBD doubling box) and thus change the polarization direction of the beam. This way we adjust the components intensities measured by the photodiodes as the laser frequency is being scanned. Once the error signal appears symmetric as in figure 3.3, we are ready to lock the cavity. Locking the cavity significantly increases the second harmonic power as the portion of light going in that is on resonance with the cavity is much higher than the passive transmission now. Part of the SHG output signal is sent to a photodiode to measure the intensity as the bottom graph of figure 3.3. Feedback signals are applied to the PZT element on the input coupler M1. When the laser lock switch is on we should not align any optics in the system any more. The system has to be in the scan mode for alignments.

3.1.4 Pound-Drever-Hall Locking

Pound-Drever-Hall locking technique is a widely used laser locking method nowadays. It is first described in the optical regime by Drever and Hall [29]. The mechanism is similar to an earlier technique invented by Pound [30] which is used to lock microwave cavities. The physics is simple: The frequency measured by a Fabry-Perot cavity is sent back to the laser itself to suppress perturbations and lock the laser modes [31]. When the laser light is hitting a Fabry-Perot cavity, the reflection intensity is apparently symmetric about the resonance wavelength, and the sign of the phase shift can be determined looking at the derivative of

the reflection intensity because it is anti-symmetric about the resonance. In this process the phase difference between the laser and the cavity is extracted and used for the error signal. In other words, the laser is locked to a reference stable FP cavity. The phase shift information is stored in the derivative of the reflected intensity. The basic scheme is below along with Saturation Absorption Spectroscopy.

As in figure 3.4, an electro-optic modulator (EOM) that is driven by an RF oscillator modulates the frequency of the laser by Ω. This signal is then sent to the Fabry-Perot cavity. It is the reflection signal from the input coupler that we are interested in because it is the signal that contains phase information and we use a photodiode to measure it. The modulated laser contains three components (see equation 3.5). When the modulated laser is off resonance with the cavity, the reflection signal coming out contains the sidebands signal generated by the modulator and the carrier which experiences a phase shift, is then sent into a mixer and compared with the frequency of the RF oscillator which drives the EOM. The outcome contains both the frequency sum and the difference of the two signals going in. It is the difference that contains phase information so that we use a low frequency pass filter to extract it and use it as error signal. There is also another photodiode used to measure the transmitted signal of the cavity as the reference of the signal outcome.

After modulation by frequency Ω, the laser field is

$$E = E_0 e^{i(\omega t + \beta \sin \Omega t)} \tag{3.4}$$

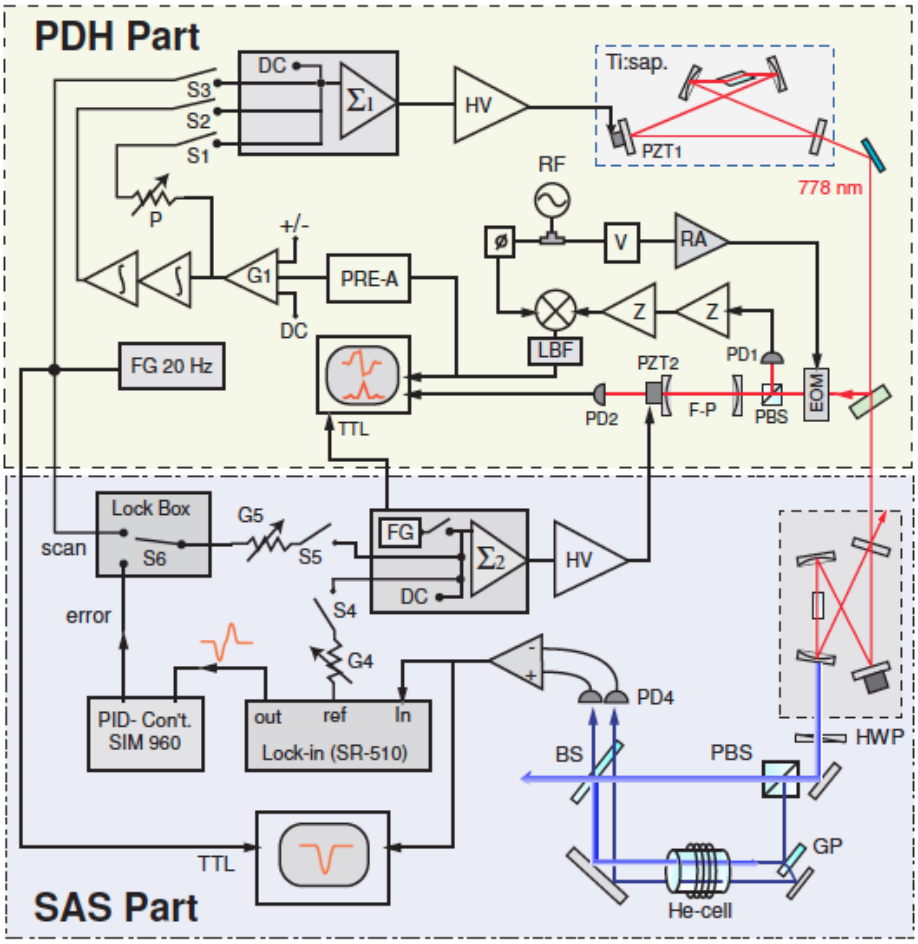

Figure 3.4: Stabilization electronics for the 389 nm blue light system [10]. As we see the major locking systems are Pound-Drever-Hall system and Saturation Absorption Spectroscopy system.

The modulated laser can be seen as a superposition of three components: A central carrier and two sidebandes. This result can be derived mathematically by the expansion of the modulation at RF frequency to a Bessel function series and only keep $n = 0, \pm 1$, the rest are all negligible on this scale.

$$E \approx E_0[J_0(\beta)e^{i\omega_c t} + J_1(\beta)e^{i(\omega_c+\Omega)t} - J_1(\beta)e^{i(\omega_c-\Omega)t}] \tag{3.5}$$

In the equation β is modulation depth (how much the modulated variable of the carrier signal varies around its unmodulated level) where in this case $\beta \ll 1$ for small modulation. Thus the terms other than n=0,$\pm$1 can be neglected. The Js in equation 3.5 are the Bessel functions. We can see that the first term involving frequency of ω_c is the carrier frequency and two sidebands with frequency of $\omega_c + \Omega$ and $\omega_c - \Omega$. After the reflection from the FP cavity, the beam outcome should contain three frequency components as well which can be expressed as

$$E_{out} = E_0[R(\omega_c)J_0(\beta)e^{i\omega_c t} + R(\omega_c+\Omega)J_1(\beta)e^{i(\omega_c+\Omega)t} - R(\omega_c-\Omega)J_1(\beta)e^{i(\omega_c-\Omega)t}] \tag{3.6}$$

where $R(\omega)$ is the reflection coefficient of the FP cavity at incoming frequency ω:

$$R(\omega) = \frac{E_{out}}{E_{in}} \tag{3.7}$$

We can not directly measure the amplitude of the reflection laser but we can measure the intensity P. The intensity result is given by $P = |E_{out}|^2$ which

is from the photodiode we mentioned on the reflection beam path. This signal contains the phase information we need. After some algebra [31], the reflection power measured can be expressed:

$$\begin{aligned} P_{ref} &= P_c|R(\omega_c)|^2 + P_s|R(\omega_c+\Omega)|^2 + P_s|R(\omega_c-\Omega)|^2 \\ &+ 2\sqrt{P_cP_s}Re[R(\omega_c)R^*(\omega_c+\Omega) - R^*(\omega_c)R(\omega_c-\Omega)]\cos\Omega t \\ &+ 2\sqrt{P_cP_s}Im[R(\omega_c)R^*(\omega_c+\Omega) - R^*(\omega_c)R(\omega_c-\Omega)]\sin\Omega t \\ &+ (2\Omega terms) \end{aligned} \tag{3.8}$$

This result contains three parts: A DC power from the carrier; Two oscillating terms at frequency Ω; Higher-order terms from the interactions between the sidebands. The Ω terms in the equation above contains the phase difference information we want to extract because it is created from interference between the carrier and the sidebands. We can see in the equation, either the sine term or the cosine term always vanishes depending on the modulation frequency [31], and the remaining term shall be the error signal. The intensity signal picked up by the photodiode is sent to a mixer with the frequency of Ω which is exactly the same signal that drives the modulator to extract the Ω frequency term in equation 3.8. The outcome of the mixer contains a small DC signal which will only appear when the incoming signals share the same frequency and a 2Ω frequency term. At this point we see that when the laser is on resonance with the cavity, there should not be any phase-shifted carrier frequency component coming out

or the side bands. Because the sidebands are symmetric about the resonance frequency and would destructively interfere with each other so the total signal should be zero. When the laser is off-resonance, the difference between the two signals that going in contains the phase difference between the carrier laser in and FP cavity. This signal, after extraction by a low pass filter, is fed back to the electronic active feedback system as the error signal.

Sample error signal and output are shown in figure 3.5 (Data from S.H.Lee in 2006). In figure 3.5 top graph we see the error signal is anti-symmetric about the resonance frequency as we expected. The error signal here is the imaginary part in equation 3.8

$$\epsilon = 2\sqrt{P_c P_s} Im[R(\omega_c)R^*(\omega_c + \Omega) - R^*(\omega_c)R(\omega_c - \Omega)] \tag{3.9}$$

.

As is in figure 3.5, the transmitting signal contains three peaks, it corresponds to the amplitude of the signal going in. The middle highest peak indicates the carrier frequency. We see that the the three slopes in the upper graph corresponding to the three peaks in the lower graph indicate where the error signal is zero as the resonance frequency, and at this frequency the sign of the error signal is about to change, and this indicates the incident light is on resonance with the cavity now. Again the error signal comes from the Ω component in the intensity outcome. We are looking to lock the signal to the resonance frequency. Technically any one of the three peaks would give us zero

error signal, but it is the middle peak that gives us the maximum power output.

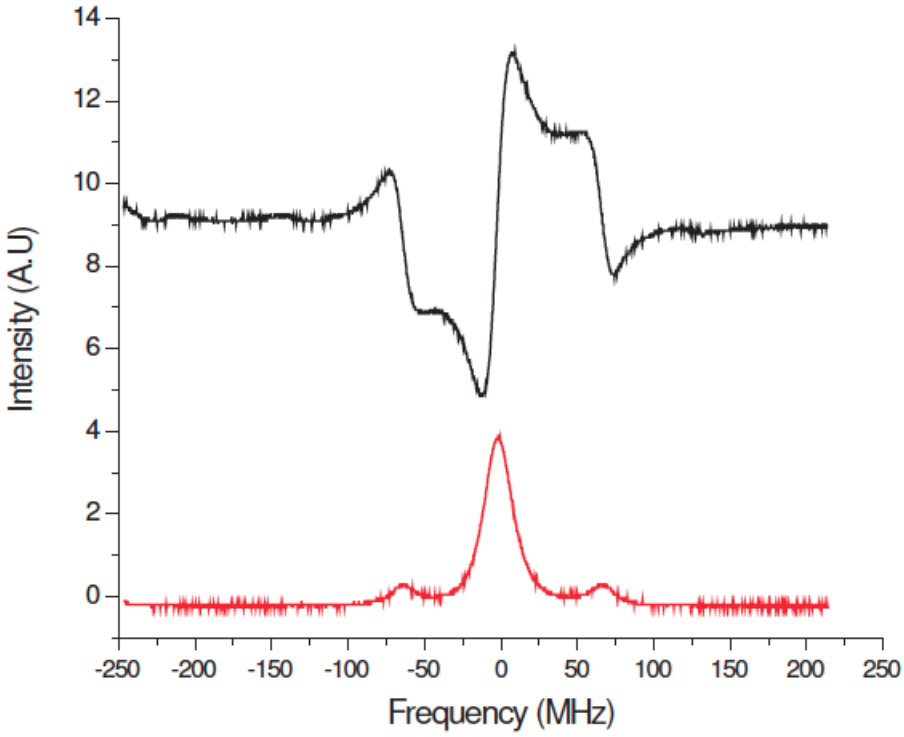

Figure 3.5: Pound-Drever-Hall error signal(top) and transmission signal through FP cavity(bottom) [10]

The error signal out of the mixer is then sent to a low noise amplifier in figure 3.4. Then a two stage integrator before being sent to a summing conjunction along with the SAS feedback signal. Finally the feedback is applied onto the PZT mirror in the Ti:Sapph cavity and stabilize the frequency.

Using the PDH lock onto the Ti:Sapph procedures are following, here I take Xiaoxu Lu's method mentioned in her thesis [11] for a brief discussion: First we

stop the FP cavity scanning by turning off the function generator that drives the signal back on to Fabry-Perot PZT, the switch is on the summing box panel. Then we adjust the DC offset to try to get the transmission signal as high and as close to the resonance height. Then we switch on the S knobs (S1 and S2) and adjust the gain to smooth the locking signal. Finally turn on the PID feedback and wait for the signal to get steady. One thing to mention is when there is multimoding in the cavity in the process as we adjust the signals, we must stop and adjust the cavity length to make sure that the wavelength readings exactly match the wanted wavelength. Sometimes the transmission signal jumps a lot which indicates that there is mode hopping in the Ti:Sapph laser. When this happens we need to turn off the whole PDH signal lock and start again.

3.1.5 Saturation Absorption Spectroscopy

In the blue laser system we already brought in two locking systems: H-C lock to lock the MBD doubling cavity and a PDH lock to lock the Ti:Sapph laser to the FP cavity. But the Fabry-Perot cavity may not be ideally stable. It slowly drifts away from the original length as temperature changes, too. We need a more stable reference to lock the PDH cavity on a longer time scale to stabilize the whole system. To do this we introduce Saturation Absorption Spectroscopy (SAS) which is considered almost not responsive to external temperature changes. It uses the atomic transition itself as the reference signal. Nowadays SAS locking mechanism is commonly used in laser locking techniques.

In stimulated emission, only light with corresponding wavelengths could pro-

duce certain transitions. Based on this we could lock the laser to the transition frequency itself. Further discussions could be found in [19].

If a laser beam passes through a cell of atomic gas and its frequency is on resonance with an electric dipole transition of the atom, apparently it will be absorbed and the transmission signal will be lowered. That means if we scan the laser frequency through the transition, we should see a "dip" on the transmission signal. Since the atoms in the cell have different velocities that would cause Doppler broadening, the actual signal dip is wider than the theoretical value.

For highly saturated pump beams (intensity is a lot larger than saturation intensity I_s) on resonance with the transition, the absorption spectral width is $\Delta\omega_{sat} = \Gamma(1+s)^2$ (Γ is the natural width and s is the saturation parameter $s = I/I_{sat}$) due to power broadening. Here I_{sat} is the saturation intensity for the specific atomic transition. If there is a weak, counter-propagating beam with the right frequency ω that is the transition frequency of the atoms, overlapping with the pump beam. Then as we scan the frequency we can see the absorption (the dip above) is reduced and the transmission signal is higher. In other word, this is a "Doppler free region", and on the graph there should be a small peak on the transmission dip. It's also known as the "Lamb dip". In our system both the pump and probe laser come from the same beam and have the same frequency. Here utilizing the Lamb dip is the key to the SAS locking system. For if the two beams are both on resonance with the transition frequency, they will interact with only one velocity group that has zero velocity. If they are off resonance, they will interact with two different velocity groups because they

are counter propagating as the atoms see different frequencies due to Doppler shifting. We will not see the reduced absorption when they are off resonance as it requires both counter propagating beams to get involved.

In our experiment, the laser out of the FP cavity goes through a beam splitter and is divided into three parts: Two weak beams (probe and reference) and a strong pump beam. The probe beam and the strong pump beam counter propagate and overlap with each other while going through the helium cell. Two photodiodes collect the output signals and send them in to the subtraction box so the Lamb dip signal is extracted. The sample figure is shown below. This signal contains the phase information and can serve as error signal which is fed back to the PZT on the Fabry-Perot cavity and is used to lock the PDH lock. We may extract the error signal by comparing the transmission signal with or without the pump beam. This way only the Lamb dip signal is reserved.

The target transition frequency is produced by a helium cell with a discharge driven by a 57 MHz oscillator, and this frequency is amplified by an RF amplifier thus the power is high enough to generate metastable helium. The saturation parameter (scales with the intensity) for the pump beam is 15 and for the probe beam is 1. As the overlapping beams and the reference beam pass the cell at the same time, the power outputs of them are measured separately by two photo detectors. The intensity signals are further compared by being sent into a signal subtraction unit. Here the relative intensity between the beams are balanced by a variable filter to make them comparable. Once we get the remaining signal (the overlapping signal subtract the probe signal), it is sent to an SRS Model

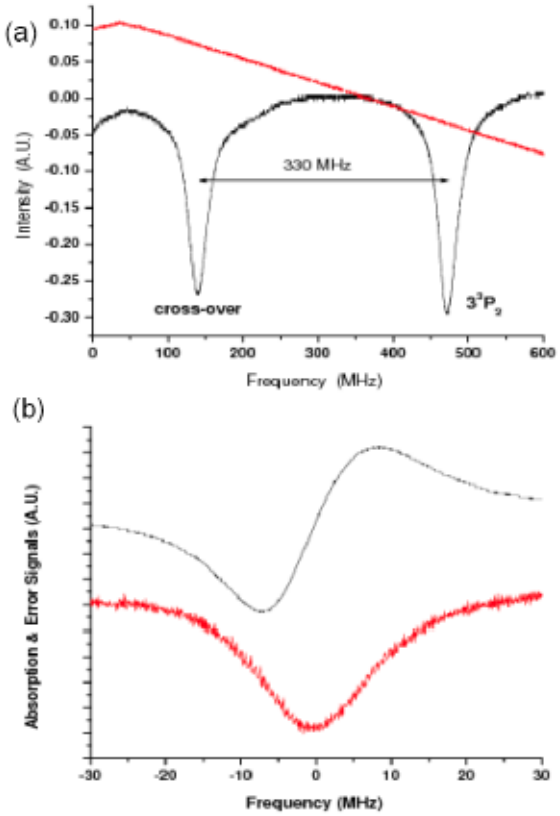

Figure 3.6: Typical SAS signals [11] as we scan the frequency.

510 lock amplifier which is modulated by an 800 Hz signal from a Model 124A function generator. We see that as the frequency is being scanned, the zero error signal point corresponds to the lowest transition signal. The generation of error signal is similar with the PDH method as in figure 3.6.b) which will not be discussed again here.

In a multiple atomic level case, we might be able to observe that there are extra peaks at unexpected positions as we see in the top graph in figure 3.6,

and these are known as "cross-over peaks" [11]. This is because the probe and pump beams may be on resonance with different transitions for different velocity groups. Figure 3.6.a) shows a typical cross-over signal of the states 3^3P_2 and 3^3P_1. To lock the laser with SAS system, we have to find the right SAS absorption peak in the scanning range. First make sure the starting wavelength is within the right theoretical range (777.951∼777.752 nm). Then turn on the scan of the Ti:Sapph cavity. The way we tell it is the right peak is that keep tuning the DC offset towards higher wavelength to find the peak with the longest wavelength. Because the target state 3^3P_2 is the lowest energy state among the J levels so it relates to the longest transition wavelength and this property here makes everything easy here. Finally we can turn on the PDH lock through the panel and lock it to the transition frequency.

3.2 ∼796 nm Red Laser System

Compared with blue laser system with three external locks, the red laser (∼796 nm laser system) is rather simple. The basic diagram is shown below in figure 3.7.

The red laser is also based on a Ti:Sapph laser but from a different manufacturer. It is a Russian made Tekhnoscan TIS-SF-777 model [32]. It is a CW, single frequency laser system with an external electronic control panel unit.

Being pumped by a Verdi laser with power at 7 W to 10 W pumping, this Ti:Sapph gives us the ∼ 796 nm (usually scanned with a range of no more than

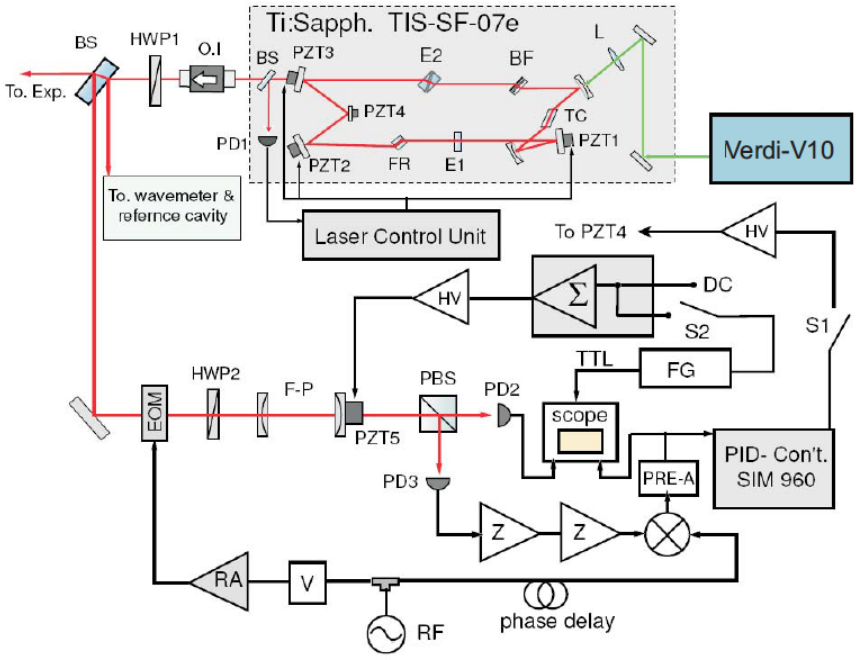

Figure 3.7: Red laser scheme [11] [32].

100 nm) infrared laser we want to use as the Stokes laser that connects 3^3P_2 and the Rydberg states in the STIRAP experiment. Compared with the SEO Ti:Sapph discussed above it is rather less efficient because it has more optics in the system. In the ring mode of the Teknoscan Ti:Sapph there are four optical elements in the path. As the frequency of the Stokes laser needs to be scanned across the Stark manifolds to be on resonance with different Rydberg states so it is connected with a function generator and being swept across a target wavelength range.

Though the Tekhnoscan laser system has a different optical arrangement, the ring mode generation is similar with the blue one. There are six mirrors in total that are involved. Two of them are spherical and the rest are plane as are in figure 3.7 (in the ring mode alignment). Aligning it usually means we need to start in the linear mode which generates standing waves and then change it into the ring mode. There are three extra mode selection tools: Thick and thin etalons and a birefringent filter. The wavelength of the laser is selected coarsely with the 3-stage birefringent filter. The filter is made of three parallel crystalline quartz plates placed within the laser cavity at Brewster's angle. It only allows light with certain range of wavelengths to pass. Within a certain spectral range when the light passes through the filter the linear polarization does not change. The way we adjust the wavelength is we rotate the filter about and axis subject to the plate. Then the output wavelength is tuned. Two Fabry-Perot interferometers–also known as etalons, are deployed. There are one thin and one thick of them. We can rotate the etalons by electronic

control. A coupling circuit can scan the transmission peak of the etalon. This way we can achieve a relative finer tuning of the wavelength. The way we control the thick etalon is to modulate the length of the Fabry-Perot cavity. Only laser frequency components on resonance with the transitions from intermediate state to the Rydberg states can pass, and it produces a variation of the intensity. This provides further refined tuning of the laser mode selection. As we mentioned, more optics in the cavity might be the reason for the relative low efficiency for the Tekhnoscan laser.

Since there is no certain wavelength to lock to because we need to sweep it through different Rydberg states with different transitions so there is no need to use SAS to lock it to a certain transition. Also we will not use H-C lock here because we do not need to double the red laser frequency, the outcome is just the wavelength for our infrared light.

The Tekhnoscan Ti:Sapph system comes with an electronic control box so it's a lot simpler to adjust compared with the SEO Ti:Sapph. We could control the unit over thick/thin etalon and the birefringent filter to select certain wavelengths and adjust the modes. Before we start using the red laser in the STIRAP experiment, the electronics are really helpful adjusting the frequency.

Usually we need a laser with the wavelength from 770 nm to 840 nm to get a decent wavelength range to cover the Rydberg states (from $n = 12$ to $n = 30$ or higher). Among the wavelength selection tools, the birefringent filter is the most coarse one. Second is the thick etalon. Both these adjustments can be achieved on the electronic panel.

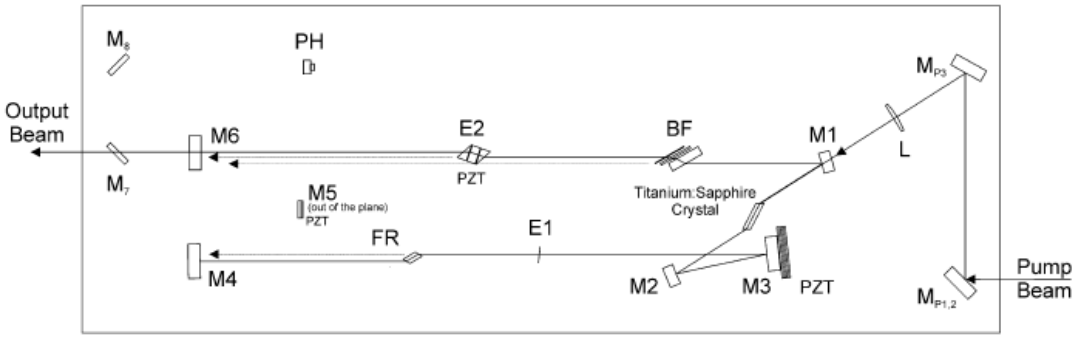

Figure 3.8: Linear generation [32]

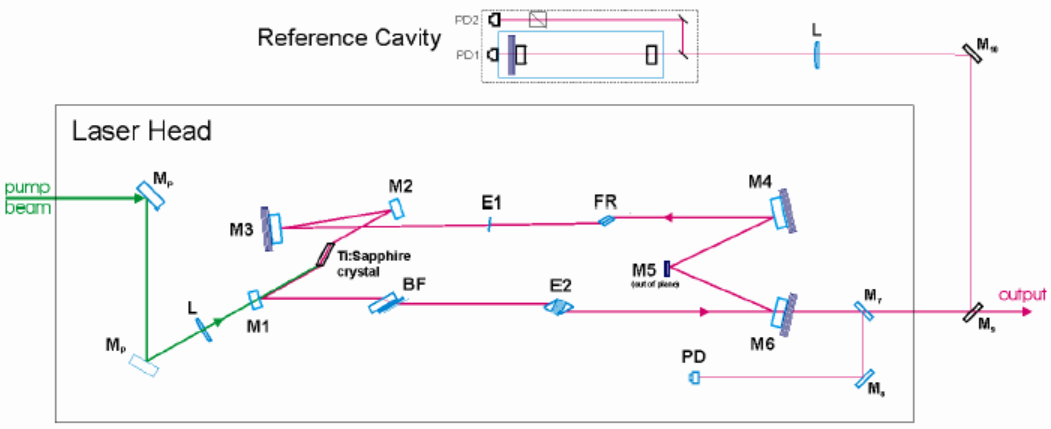

Figure 3.9: Ring generation [32]

The Tekhnoscan Ti:Sapph needs to be locked, too. The mechanism of the lock within is similar to the PDH lock we use in the blue laser locking, which we will not discuss here. The thick etalon will be subject to a modulation signal. The signal is compared with the original frequency and send into a mixer. After a low frequency pass only the signal difference will be measured and is used as the reference to create an error signal.

3.3 1083 nm Laser

In the STIRAP map, the 389 nm blue laser connects the 2^3S_1 state and the 3^3P_2 state and the red laser connects the 3^3P_2 state and the Rydberg states. But under most circumstances not all the metastable atoms will get excited (actually only a small portion will get involved in the STIRAP experiment). For the SSD detector to pick up signals, we need to separate the remaining metastable atoms and Rydberg atoms. The way we achieve this is we add a 1083 nm laser several centimeters (which can be changed as we need to vary it as a changing parameter in the measurements) downstream in the beam. The laser with this wavelength will connect 2^3S_1 to another intermediate state: The 2^3P_2 state. This way, the metastable atoms will be given a deflection that they can be picked up separately from a different position apart with Rydberg signals by the SSD detector.

We use a SDL-6702-H1 distributed Bragg reflector diode laser to produce the 1083 nm laser for metastable deflections. We also use the SAS locking feedback

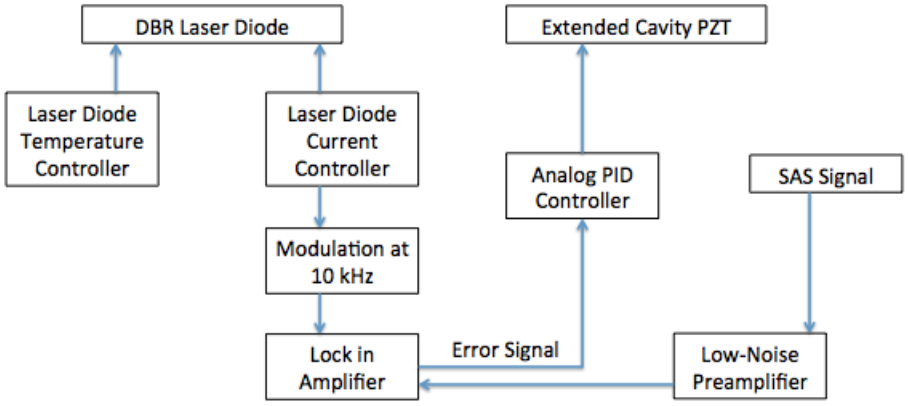

Figure 3.10: Basic electronics of SAS feedback system.

system to lock this laser to the 2^3S_1 to 2^3P_2 transition. The diode is packaged in an eight-pin TO-3 window mount with a thermistor and a thermoelectric cooler. The temperature is kept stable at $21.9 \pm 0.1°C$ by an ILX Lightwave LDT-590 temperature controller and the current of the laser diode is set with a Thorlabs LDC 500 laser diode controller. The actual linewidth of this diode laser is a little wider than the natural wavelength and we may narrow it by introducing an extended optical cavity and this also helps stabilize the laser frequency as is in figure 3.11 below. We set up the cavity and put a Polystyrene foam insulation to protect it from exterior temperature fluctuations. The laser output is separate into two beams: Roughly 70% goes into the experiment and is used to push away the metastable atoms. About 21% is sent into the SAS locking system to lock the frequency. In the SAS locking system, the feedback signal has to be first amplified by an Stanford Research System (SRS) SR560 preamplifier and then

by an EGG Princeton Applied Research lock-in amplifier as the figure indicates. To generate an error signal from the SAS lock, we have to induce a modulation signal. In this case we use an SRS DS345 function generator to generate a 10 kHz signal which also serves as the reference signal for the lock-in amplifier. The error signal is then sent to an Analog PID controller and to the PZT in the cavity. Faraday isolators are deployed in both of the two paths. The basic electronic setup map is shown below. They are to prevent disruptive feedback to the system. The light contains two spectrum components $(\omega + \delta, \omega - \delta)$ and $(\omega, \omega + 2\delta)$ and the first one we are using is the first component. Letting the beam double pass the acousto-optic modulator(AOM) can achieve that [24]. Here the AOM is driven at a frequency $\delta/2\pi$.

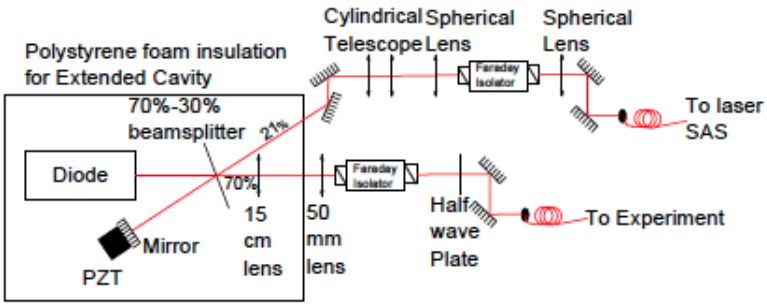

Figure 3.11: 1083 nm laser system scheme map [11].

This 1083 nm laser will separate the remaining metastable atoms for us to detect. The mechanism will be later discussed. This way by using the SSD detector to measure the transverse signal distribution with the 1083 nm laser

on or off, we could read the efficiency of the STIRAP.

3.4 Laser Alignments

We have introduced how the laser systems work, this section will be mainly about testing and aligning the systems. So far this is really a factor that delays the research progress. Hopefully our efforts in this can help the future members in this program. This process is mainly done by Mr. Zakharov, Mr. Mckenna, Ms. Gasparik, and me.

In late 2014 the power coming out of the red Ti:Sapph went really low (~ 0.6 W with pumping power 10 W) so we decided to clean the optics and realign it, and a hole was found burnt on the pump mirror in the Ti:Sapph (the starting mirror where the Verdi pumping laser goes in). So we had to open the whole box, replace the mirror and realign it from scratch. The basic rules are to follow the optical path and maximize the power output. We tune the length of the cavity by adjusting mirrors and of course to make sure the optics in the right vertical and horizontal position. This is better finished within a short time because the optics may slowly drift away from the right angle and position. We first take out thick and thin etalon, birefringengt filter, focusing lens and Faraday rotator (in linear mode, of course). The PZT mirrors are old and rather hard to adjust so what we did was we found two auxiliary mirrors with a small transmission coefficient place them at where the PZT mirrors was, then adjust to make the spot appear in the right position. In the linear mode, we make M_4 and M_6 in

the cavity reflect the laser back to their own paths to create standing waves and in this mode it doesn't involve mirror M_5 which is out of the linear mode plane. Then we align them without the selection optics and try to get as much power output. In this process we used an extra IR viewer to locate and follow the fluorescent spot. Then we put everything back in, switch the system to ring mode and align again to maximize the power. As a matter of fact, the last step just guarantees that we have the maximum power in linear mode and the position and angle of M_4 and M_6 are totally different with what are in the ring mode. Furthermore once we add the Faraday rotator and the thick etalon, they will horizontally shift the optical path away which is rather noticeable so we're expecting to see a position change of the fluorescent spot and adjust the cavity again to make the spot hit M_4 and M_6 again. The ring mode map is different from the linear mode and both of the schemes are provided below. Usually after we get a decent amount of light in the linear mode we're ready to switch it into ring. Thanks to Mr. Sergey Kobstev we are able to get the outcome around 1.3 W$\sim$ 1.4 W in January 2015. The steps we take to start the laser in ring mode is simple: Instead of letting beams overlap with themselves bouncing back from M_4 and M_6, we get the PZT mirror M_5 involved in the path and the beam should hit the mirrors in the following order: $M_4 \rightarrow M_5 \rightarrow M_6$. As the Ti:Sapph manual [32] shows.

There are a few tips to follow when aligning the red Ti:Sapph:

First, we need to keep all the optics at the height of 62 mm. A good IR viewer is needed to keep track of the fluorescent spot. Second, when we change

the system from linear mode to ring mode, be sure that the holders fits the angle. We could introduce plane mirrors with small transmissions if necessary. At last, the biggest impact on the signal will come from the thick etalon. We need to align it first before everything.

Chapter 4

STIRAP Theory

4.1 Introduction

Coherent excitation of atoms has been a key issue in AMO physics for several decades [33]. In our experiment we want to excite metastable helium atoms (2^3S_1) to high quantum number Rydberg states in a two steps process and maximize the efficiency of the population transfer. The Rydberg atoms are the ideal tools for various applications in atomic physics because of their unique properties (See Chapter 1). Here Stimulated Adiabatic Raman Passage, for maximizing the efficiency of Rydberg atoms creation, is introduced.

We start off by introducing a two state model before our three level helium excitation. In the process of exciting a two state atom in an incoherent field, the population of the higher state is limited by the spontaneous emission and stimulated emission. The prediction of the maximum population transfer ratio

was first made by Einstein [34]. When the incoherent radiation intensity is sufficient and the field frequency is near the atomic resonance frequency, the population or probability of the excited state at time t can be calculated from the Einstein Coefficients [33]

$$P_e(t) = \frac{1}{2}(1 - \exp[-B \int_0^t u(t')dt']) \tag{4.1}$$

where $u(t')$ is the spectral energy density and B is Einstein Absorption Coefficient. We can see that under this circumstance that the atom is interaction with an incoherent field, the maximum efficiency could not go over 50% as figure 4.1 shows.

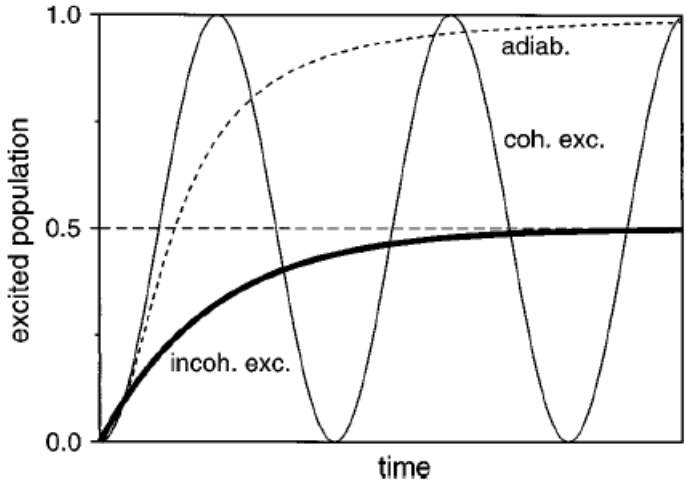

Figure 4.1: Excited state population in a two level state system [33]

For a coherent field, the result is different. Equation 4.1 no longer applies to the situation. The population or the probability of the excited state has to be derived by solving the Schrödinger's Equation as probability can be acquired

by $P_n = |C_n|^2$:

$$-i\hbar\frac{d}{dt}C_n(t) = H(t)C_n(t) \tag{4.2}$$

Here the Hamiltonian H represents the interaction between the atom and the field. The coherent field can be considered as a monochromatic field $\vec{E} = \vec{\varepsilon_0}\cos(\vec{k}\cdot\vec{r} - \omega t)$. Here the population is oscillating between the two states [10]. The frequency of the oscillation generated by a certain coherent light field is defined as the Rabi Frequency [35] [36]:

$$\Omega = -\frac{e}{\hbar}|\vec{\varepsilon_0}|\langle e|r|g\rangle = -\frac{\mu\varepsilon_0}{\hbar} \tag{4.3}$$

in which e and g stand for excited and ground state of the system, and $\mu = e\langle e|r|g\rangle$ is the dipole transition moment which depends on the quantum states involved. Here we see that the Rabi frequency depends on the field intensity and the transition moment. For equation 4.2, the Hamiltonian of a typical atom-field interaction is given by [37]

$$H = H_0 + H' = \hbar\begin{bmatrix}\omega_g & 0\\ 0 & \omega_e\end{bmatrix} + \hbar\begin{bmatrix}0 & \Omega\cos\omega t\\ \Omega\cos\omega t & 0\end{bmatrix} \tag{4.4}$$

ω_e and ω_g stand for the atomic enegy corresponding frequency and ω is the external field intensity. We can express the solution using the Rabi Frequency [37]:

$$P(t) = \frac{1}{2}[1 - \cos\Omega_{eff}t] \tag{4.5}$$

where Ω_{eff} is the effective Rabi frequency which depends on the detuning. Theoretically the maximum transfer efficiency could be 100% [37] as the population keeps being exchanged between the two states. At this point the average efficiency is 50%. That is based on the condition that the laser is precisely on the resonance frequency of the quantum states. But when there is a frequency detuning Δ in experiment, the maximum efficiency is lowered. At this point the effective Rabi frequency is no longer Ω, instead it is $\Omega_{eff} = \sqrt{\Omega^2 + \Delta^2}$. And the maximum efficiency is $(\Omega/\Omega_{eff})^2$ instead of 100% [33], and the oscillation period is shorter as the atoms oscillate faster.

A robust method to achieve a higher efficiency is Adiabatic Rapid Passage which is known as ARP. In this method the frequency of the external field is slowly tuned from below resonance to above resonance. This way it is scanned across the resonance point. The time scale of this frequency sweeping process shall be slower than the Rabi frequency but faster than the spontaneous emission rate. This way we manage to achieve an "adiabatic" condition. In the Bloch Sphere picture, the state vector will always stay within the "$U = 0$" plane and move to the north pole. We can see in figure 4.1 above that through this adiabatic method, we could try to maximize the efficiency of this excitation process and the population is not resonating between the states as it is slowly being pushed to the maximum by the ARP. The detailed mechanism and performance have been discussed in previous theses [38] [39].

4.1.1 Power Broadening Effects

In the first two levels in the excitation process, the transition is driven by force produced by the pump laser. When it is on resonance with the transition, due to the power broadening effect introduced in the SAS section, the maximum force deployed and the helium velocity change will be increased.

The resonant force produced by the pump laser can be expressed as:

$$F = hk\gamma'/4\pi \tag{4.6}$$

Since the power broadened linewidth is

$$\gamma' = \gamma\sqrt{1+s_0} \tag{4.7}$$

We may measure the transverse position difference as we turn on or off the pump laser. As it could be mapped:

The square of the helium velocity change fits the blue power pretty well. And this measurement corroborate the result that the pump laser force has a linear relationship with the saturation parameter.

In this measurement process the credits go to Mr. Casey McKenna and Ms. Jessica Casparik, who generously share the data.

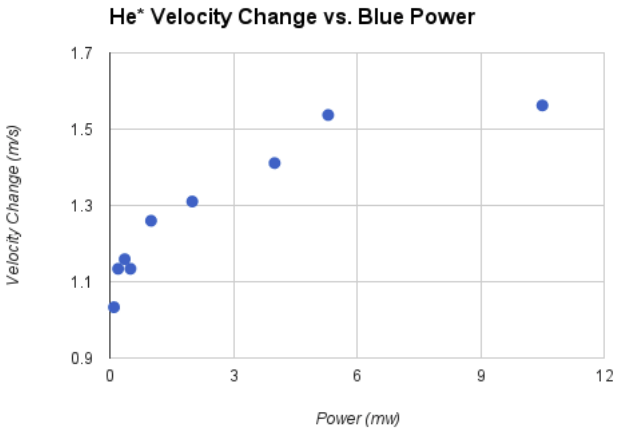

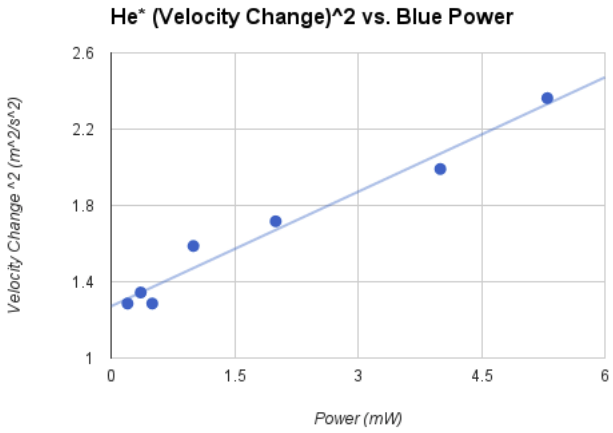

4.2 Stimulated Raman Adiabatic Passage

In a three level system, two individual coherent lasers with corresponding frequencies are to connect three successive states, on a two photon resonance [11]. In our case, we try to excite the metastable helium atoms to Rydberg states via an intermediate state. As we introduced in the apparatus chapter, the metastable helium is created by an electric discharge of 19.8 eV. As the ladder system in figure 4.2 below shows, the transition process starts from the lowest energy state $|1\rangle$. The pump laser with appropriate frequency (389 nm)

interacts with the atom and excites it onto level $|2\rangle$. Then the Stokes laser (790∼830 nm) further connects it to the final state $|3\rangle$.

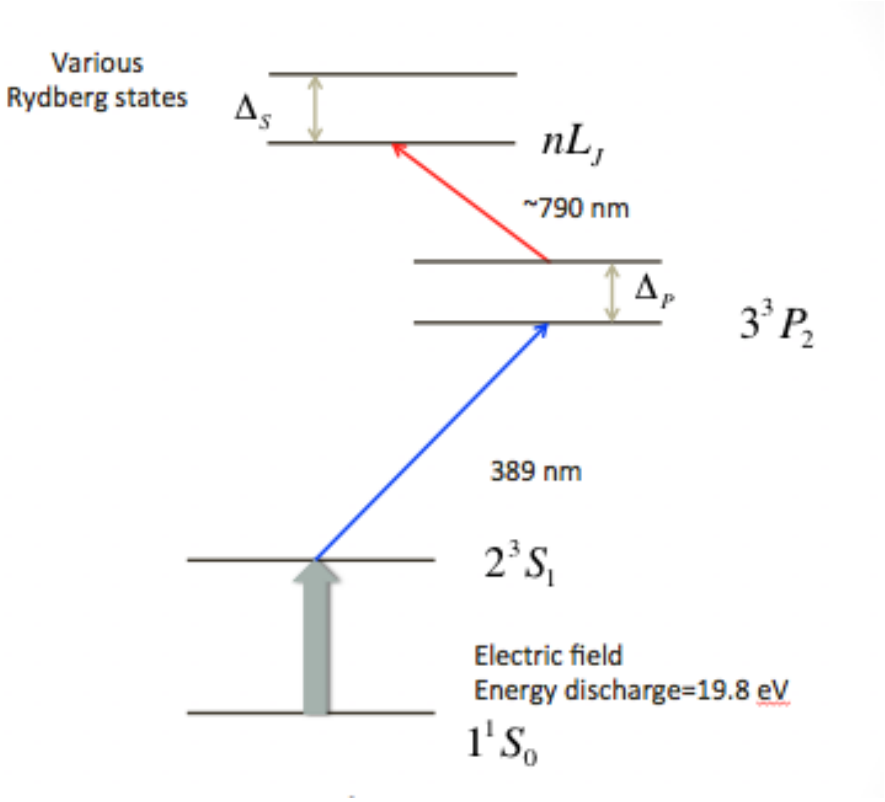

Figure 4.2: Excitation of a three level system.

In the traditional method, the pump laser and Stokes laser are deployed in an intuitive order: $|1\rangle$ to $|2\rangle$, $|2\rangle$ to $|3\rangle$. This sounds reasonable but there is one problem limiting the excitation efficiency–the stimulated emission of the intermediate level $|2\rangle$. Even if we achieved the best efficiency, the average transferred population will not go above 50%. Any atoms excited from state $|1\rangle$ to the intermediate state will experience a population redistribution again and this way the theoretical highest population ratio of the state $|3\rangle$ is only 25%. In the

ladder system in figure 4.2, Δ_P and Δ_S stand for the detunings of the two lasers (as they might be above or below resonance).

The STIRAP method stands for Stimulated Raman Adiabatic Passage which is a particular population transfer process between different quantum energy levels. The theory was first proposed by Hioe and Eberly [40] in 1981, and the first experiment was achieved by K. Bergmann et al. in 1988 [41] and in a subsequent paper in 1990 [42]. Here we will briefly discuss the STIRAP mechanism based on our three level helium excitation system.

The interesting feature of this special method is that in the experiment the Stokes laser driving the second transition ($|2\rangle$ to $|3\rangle$) which connects the intermediate state and the highest state actually interacts with the atoms before the pump laser (the laser that drives $|1\rangle$ to $|2\rangle$). For a given interaction between atom and field, we can have the Hamiltonian and the related Schrödinger's Equation. With rotating wave approximation we find [43]

$$H = \frac{\hbar}{2}\begin{bmatrix} 0 & \Omega_P(t) & 0 \\ \Omega_P(t) & 2\Delta_P & \Omega_S(t) \\ 0 & \Omega_S(t) & 2(\Delta_P \pm \Delta_S) \end{bmatrix} \tag{4.8}$$

And Schrödinger's Equation

$$i\hbar\frac{d}{dt}\varphi = \hat{H}\varphi \tag{4.9}$$

where Δ_S and Δ_P are the detunings of the Stokes and pump laser. In the

equation, they are defined as $\Delta_S = E_3 - E_2 - \hbar\omega_S$ and $\Delta_P = E_2 - E_1 - \hbar\omega_P$, and ω_S and ω_P are the frequencies of the pump and Stokes laser. In a ladder configuration the sign of the last element in the matrix should be plus which is our case of the three level helium, whereas in a lambda configuration it should be minus. In the two photon resonance we have $\Delta_S = \Delta_P$ hence the last term in the Hamiltonian matrix should vanish $\Delta_P - \Delta_S = 0$, and we express $\Delta_P = \pm\Delta_S = \Delta$. In this case, we may have the eigenstates and the eigenvalues of the given Hamiltonian.

$$\begin{cases} |\alpha_+(t)\rangle = \sin\theta\sin\phi|1\rangle + \cos\theta|2\rangle + \cos\theta\sin\phi|3\rangle \\ |\alpha_0(t)\rangle = \cos\theta|1\rangle - \sin\theta|3\rangle \\ |\alpha_-(t)\rangle = \sin\theta\cos\phi|1\rangle - \sin\phi|2\rangle + \cos\theta\cos\phi|3\rangle \end{cases} \tag{4.10}$$

In the equations the angle θ and angle ϕ are defined as

$$\begin{cases} \tan\theta = -\frac{\Omega_P}{\Omega_S} \\ \tan 2\phi = -\frac{\sqrt{{\Omega_P}^2+{\Omega_S}^2}}{\Delta} \end{cases} \tag{4.11}$$

And the corresponding instantaneous energies are

$$\begin{cases} \omega_+(t) = \Delta + \sqrt{\Omega_P(t)^2 + \Omega_S(t)^2} \\ \omega_0(t) = 0 \\ \omega_-(t) = \Delta - \sqrt{\Omega_P(t)^2 + \Omega_S(t)^2} \end{cases} \tag{4.12}$$

We immediately see that the second eigenstate $|\alpha_0\rangle$ has no term involving the mid-level $|2\rangle$. This is interesting because the efficiency limitation of the traditional method is the emission of the intermediate state $|2\rangle$. The instantaneous state vector can be expanded as superposition of dressed states $|\alpha_+\rangle, |\alpha_0\rangle, |\alpha_-\rangle$, and if the condition can be satisfied that our state vector can be tied with $|\alpha_0\rangle$ and the intermediate state never gets populated, or at least not much, we could "skip" the state $|2\rangle$ and populate the final state $|3\rangle$ efficiently.

The state $|\alpha_0\rangle$, known as the "trapped state", falls into state $|1\rangle$ when $\cos\theta = 0$, and falls into state $|3\rangle$ when $\sin\theta = 0$. This way we can make θ evolve from 0 to $\pi/2$ and connect the two states. To achieve this, we have to control the Rabi frequencies to meet the condition

$$\begin{cases} \frac{\Omega_P(t\to 0)}{\Omega_S(t\to 0)} = 0 \\ \\ \frac{\Omega_S(t\to \infty)}{\Omega_P(t\to \infty)} = 0 \end{cases} \tag{4.13}$$

as $|\alpha_0\rangle_{t=0} = |1\rangle$, $|\alpha_0\rangle_{t=\infty} = |3\rangle$. This indicates that the Stokes laser field will interact with the atoms first. As shown in figure 4.3 [42] below.

Theoretically in the region where there is only the Stokes laser, the Rydberg states will not get populated until the pump laser starts to get involved in the system. The mechanism is similar to electromagnetic induced transparency (EIT). When the pump laser starts to emerge and is weak at the beginning and the Stokes laser is very strong, the pump laser will not cause stimulated emission from $|2\rangle$ to $|1\rangle$ and in the Hilbert space picture, at this moment the state vectors $|\alpha_+\rangle$ and $|\alpha_-\rangle$ begin to split as the energy difference grows. At

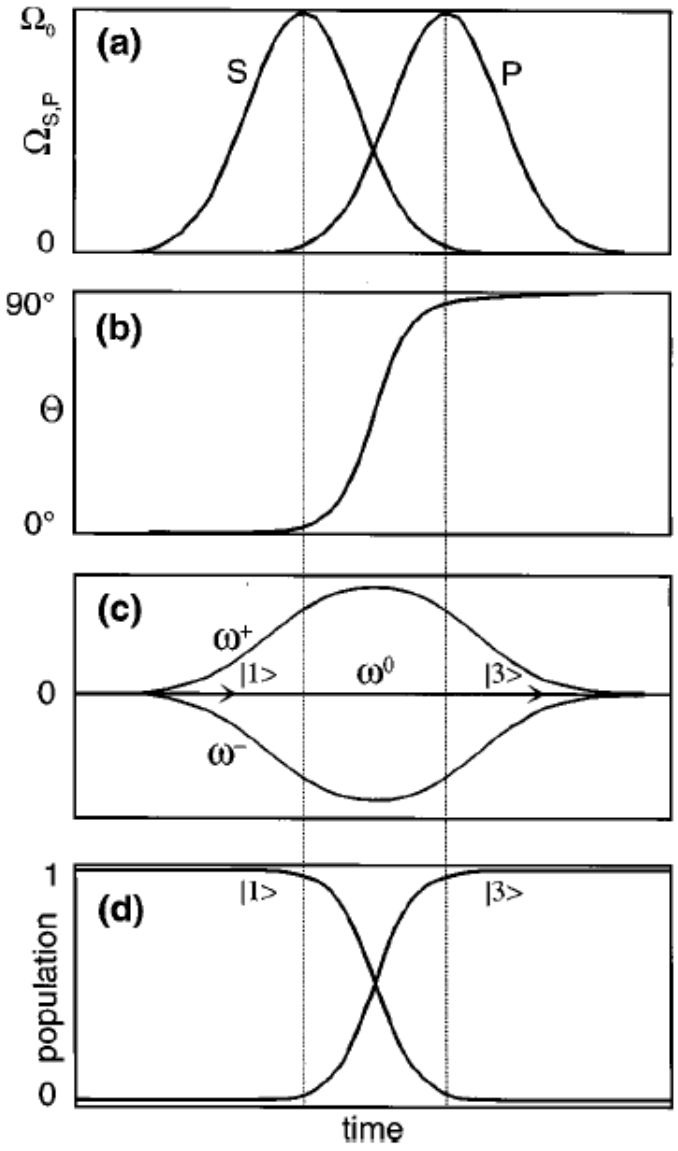

Figure 4.3: Laser field and population transfer in STIRAP [42]. a) Stokes and pump laser frequencies; b) Mixing angle Θ; c) Dressed states; d) Population of states $|1\rangle$ and $|3\rangle$

this time there is no population transfer as mixing angle θ is still 0. Then as pump laser starts to grow (the overlapping region), θ begins to move to $\frac{\pi}{2}$ and

the state vector is moving towards the north pole (state $|3\rangle$) and rotating about the U axis in the Hilbert space. In this region the energy splitting between $|\alpha_-\rangle$ and $|\alpha_+\rangle$ gets maximum. At last in the region where the Stokes is weak and pump laser is strong, the Stokes laser will not cause emission from $|3\rangle$ to $|2\rangle$ and the angle θ slowly approaches $\frac{\pi}{2}$ as Stokes laser fades and pump laser gets to its maximum value.

In the three state picture, to ensure there is no $|2\rangle$ state gets populated, the dressed state vector will have to be maintained to always move within the plane of $|1\rangle$ and $|3\rangle$ as it approaches the north pole, as figure 5.4 indicates. The vector moves from the starting state $|1\rangle$. If there's a detuning (and always will be), the vector will be slightly out of the plane and there will be a component on $|2\rangle$ direction. This requires us to satisfy a certain condition called "adiabatic following" to couple the state vector in the plane well enough and ensure maximum efficiency.

4.3 Adiabatic Conditions for STIRAP

We already introduced that to maximize the efficiency of STIRAP, we have to try to make sure that the system stays adiabatic. Any passage that involves states $|1\rangle$ and $|3\rangle$ without populating state $|2\rangle$ is considered non-adiabatic here. Look at figure 5.4 again and we are trying to make the state vector within the $U = 0$ plane. The Hamiltonian matrix element for non-adiabatic coupling between state $|\alpha_0\rangle$ and $|\alpha_\pm\rangle$ is given by $\langle\alpha_\pm|\dot{\alpha}_0\rangle$ and we can consider the process

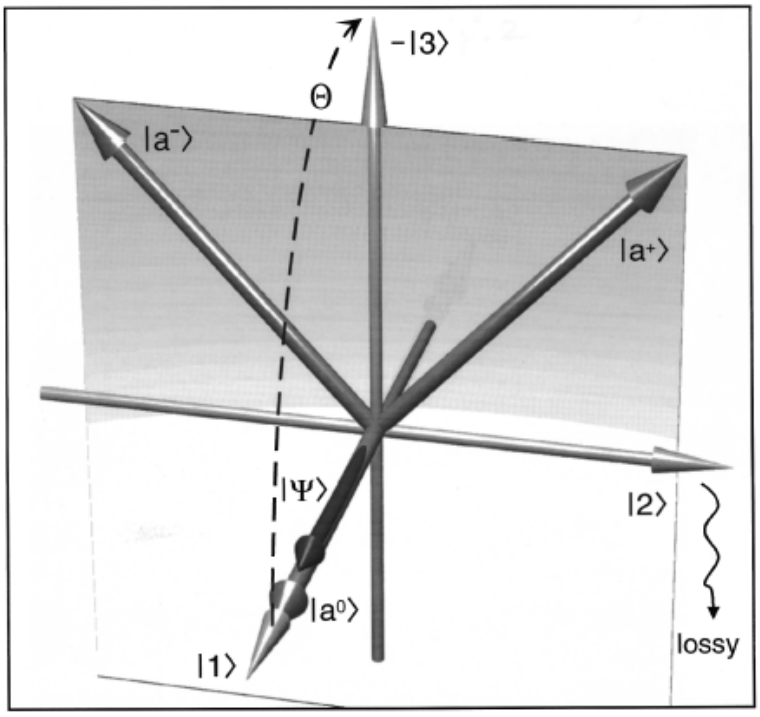

Figure 4.4: Three level STIRAP in a 3D model [42].

adiabatic if this element is small enough compared with the field induced energy splitting $\hbar(|\omega_{\pm} - \omega_0|)$ [42].

Plug in the solutions to equation 4.10 [12] to express the non-adiabatic coupling strength, we see

$$\begin{cases} |\langle \alpha_+ | \dot{\alpha}_0 \rangle| = -\dot{\theta} \sin\phi \\ |\langle \alpha_- | \dot{\alpha}_0 \rangle| = -\dot{\theta} \cos\phi \end{cases} \tag{4.14}$$

Then plug in equation 4.11 we can see the adiabatic condition is simplified to

$$|\dot{\theta}| \ll |\omega_{\pm} - \omega_0| \tag{4.15}$$

This equation describes the adiabatic condition of the evolution of the dressed state. As long as the equation above holds, non-adiabatic terms are small and the system stays under adiabatic condition. This is further expressed as [42]

$$|\dot{\theta}| \ll \Delta \pm \sqrt{{\Omega_S}^2 + {\Omega_P}^2 + \Delta^2} = \Omega_{eff} \tag{4.16}$$

Again we plug in 4.11:

$$|\dot{\theta}| = |\frac{\dot{\Omega}_P \Omega_S - \dot{\Omega}_S \Omega_P}{{\Omega_P}^2 + {\Omega_S}^2}| \tag{4.17}$$

To sum up the adiabatic condition:

$$|\frac{\dot{\Omega}_P \Omega_S - \dot{\Omega}_S \Omega_P}{{\Omega_P}^2 + {\Omega_S}^2}| \ll \Delta \pm \sqrt{{\Omega_S}^2 + {\Omega_P}^2 + \Delta^2} \tag{4.18}$$

As we can control the laser intensity and select the invovled states to adjust the Rabi frequency, we may satisfy the adiabatic condition. The result above is just a local condition at a certain time t. As both of the lasers we are using are Gaussian lasers. If we consider the time that the atoms interacting with the lasers is T, and the total mixing angle change θ of the interaction time is $\frac{\pi}{2}$, and we can see

$$\langle \dot{\theta} \rangle = \pi / 2T \tag{4.19}$$

So the adiabatic condition is

$$\Omega_{eff} T \gg \frac{\pi}{2} \tag{4.20}$$

and from experience it is better that this value is greater than 10 [11].

As we deploy the lasers in a counter-intuitive order, the overall efficiency is dependent on the overlap of the two laser beams. The two laser beams in our experiment travel in the same direction and the spatial distance between them is tunable (detailed in the chapter about laser system scheme) so we could adjust their overlapping time. Another object of having a distance between the lasers is we are trying to create a time delay and tie the initial state $|1\rangle$ as much with the trapped state $|\omega_0\rangle$ for it is the only part that gets involved in the efficient transfer.

Chapter 5

Rydberg Atoms Detection and Interaction between Blackbody Radiation and Rydberg Atoms

5.1 Introduction

In Chapter 2 we introduced that the ion detector in the interaction chamber detects Rydberg atoms by picking up their ion signals. How Rydberg atoms can be ionized has drawn attention of many researchers in the last 30 years. In

general, an atom can be ionized through collisions with other atoms, molecules, and ions, or through interaction with an external field. The binding energy for our high principle quantum number Rydberg atoms is so low that the blackbody radiation field is sufficient to ionize them even without an applied external electric field, and we could use this property for their detection. In this chapter, we briefly discuss the mechanism of blackbody ionization of the Rydberg helium atoms in our experiment and how we utilize this to detect Rydberg atoms. At the end we draw a STIRAP map of the n=24 Rydberg states based on the ion signals.

5.2 A Little History of Blackbody Radiation on Rydberg Atoms

The blackbody radiation (BBR), as one type of electromagnetic radiation, is defined as the emission coming from any heated object, and the radiation intensity would scale with temperature. In 1978, Gallagher and Cooke [44] [45] discovered that at the room temperature (around 300 K), blackbody radiation has a strong impact on Rydberg atoms. One of the most interesting thing they found is that *not only do Rydberg atoms get directly ionized through blackbody radiation, they also rapidly diffuse into nearby Rydberg states* [45]. Later in 1981, P.R.Koch [46] ran a series of tests at different temperatures in which he demonstrated that there is a dependence of the state distribution on time of exposure to the radiation as well as on temperature. In the paper by John

Farley and William Wing in 1981 [47], the concept that the depopulation of the original Rydberg state was introduced. In that paper, great details about the AC Stark shift and population redistribution among other states of hydrogen, helium and alkali-metal Rydberg atoms were discussed.

The ionization object in our experiment is helium Rydberg atoms, and the theoretical transition rates and ionization rates related to our system come from calculation done by Glukhov et al [48]. In a previous paper by Xiaoxu Lu, Yuan Sun and Harold Metcalf [49], the authors, using the system discussed in previous chapters in this article, determined that the cause of ionization was the BBR, and a nice Rydberg spectroscopy was mapped by them based on this ion detection. It is the main method of Rydberg detection in this STIRAP experiment and we will discuss this later in this chapter.

5.3 Blackbody Radiation Induced Ionization and Transitions

The theory of blackbody radiation that any hot object will emit electromagnetic radiation is well known to us. The famous Planck's law

$$I(\omega, T)d\omega = \frac{\hbar\omega^3}{\pi^2 c^3} \frac{1}{\exp(\hbar\omega/k_B T) - 1} d\omega \tag{5.1}$$

describes the blackbody radiation. The room temperature in our lab is usually around 300 K. One would conventionally imagine that the BBR at this temper-

ature would barely have any impact on Rydberg helium atoms, but it turns out the interaction between the BBR and Rydberg atoms can make a significant difference at the room temperature. We can have a sense of this by first writing down the average photon occupation number per mode $\bar{n}$ in the BBR process to re-express equation 5.1 as

$$\bar{n} = \frac{1}{\exp(\hbar\omega/k_B T) - 1} \tag{5.2}$$

We see at $\sim$ 300 K, $\bar{n} \approx 10$ for Rydberg transition with a frequency on the Terahertz scale at the room temperature [12]. It is enough to generate a much more significant transition rate than spontaneous emission ($n_{sp} = 1$). For typical neighboring helium Rydberg atoms, $k_B T \gg \hbar\omega$. We can see that the BBR is fully capable of causing excitation and decay between states, and the Rydberg-to-Rydberg transition rate from $|nl\rangle$ state to $|n'l'\rangle$ state is given by [48] in terms of oscillator strength $K_{n'l',nl}$ [12]

$$K_{n'l',nl} = 2\bar{n}\alpha^3\omega^3_{n'l',nl}|\bar{f}_{n'l',nl}| \tag{5.3}$$

in which

$$\bar{f}_{n'l',nl} = \frac{2}{3}\omega_{n'l',nl}\frac{max(l',l)}{2l+1}\langle n'l'|r|nl\rangle|^2 \tag{5.4}$$

is the oscillator strength of the transition between selected states.

As the BBR drives Rydberg atoms to adjacent states, it also ionizes Rydberg atoms. The BBR induced ionization rates of helium atoms were given in

[48]. The calculated rates for nP series are demonstrated in figure 5.1. The data comes from Yuan Sun's thesis in 2014 [12]. It gives us a sense of the transition rates and ionization rates induced by the BBR of hydrogen atoms at room temperature. Figure 5.1 shows the absolute transition/decay/ionization rates. If we take the spontaneous emission rates of different states into account, we can see the relative rates (absolute transition/decay/ionization rates over spontaneous rates) increase with the principle quantum number [48].

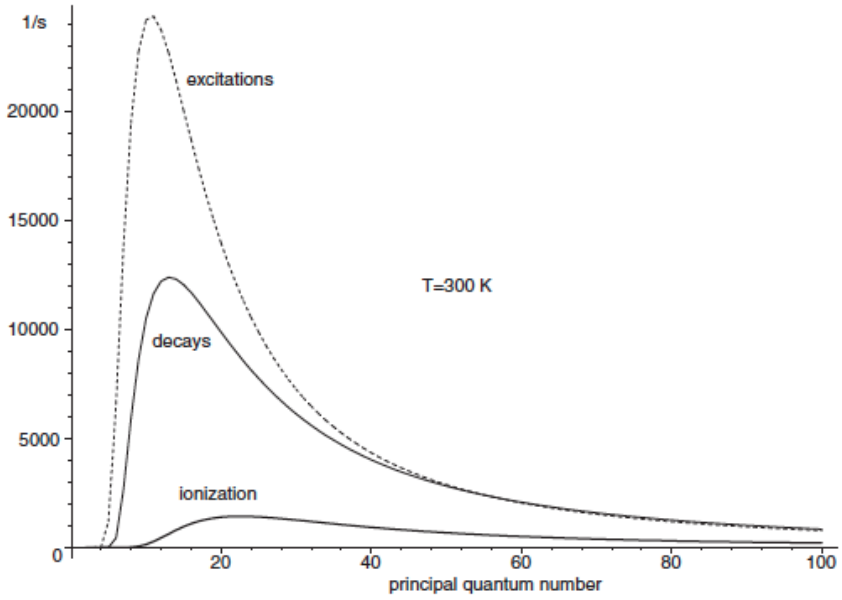

Figure 5.1: Calculated transition rates created by the BBR. The graph shows: Decay rates (thin solid curve), excitation rates (dashed curve) and ionization rates (thick solid curve) for the nP series of hydrogen atoms at T=300 K [12] [48].

Later we will come back to this ionization rate part and discuss the measurement of the rates of Rydberg atoms in our system.

5.4 Verifying the Ionization Mechanism

5.4.1 Ion Detection

We already introduced the ion detector in the detection chamber in our system. Now we will discuss the detailed working mechanism of this ion detection process.

As is shown in figure 5.2, the ion detector currently sits on the top field plate in the interaction chamber. It can be moved if necessary. The two laser beams cross the atomic beam and excite the metastable atoms to Rydberg states in the middle of the field plates. The field intensity is tunable as well as the red laser frequency. This setup is for scanning across different Rydberg states in the Stark map as there will be Stark splitting in $l \neq 0$ states with the presence of external fields.

In early experiments the ion detector used to sit at position A, the edge of the top field plate. But we can not implement field ionization experiment (we will get to it in the following section) with this setup so it is moved to position B and the top field plate is replaced with an aluminum piece with an array of about thirty small holes on it. The ion detector is put directly above the holes so the ions could fly through the holes and get picked up by the ion detector. One thing to be noted is that when the field plates are not grounded, the ion detector can only detect the ions that are produced right below the ion detector position. For the ions before the ion detector, even if the field intensity is small, they will be attracted immediately and fly towards the plate and the time it

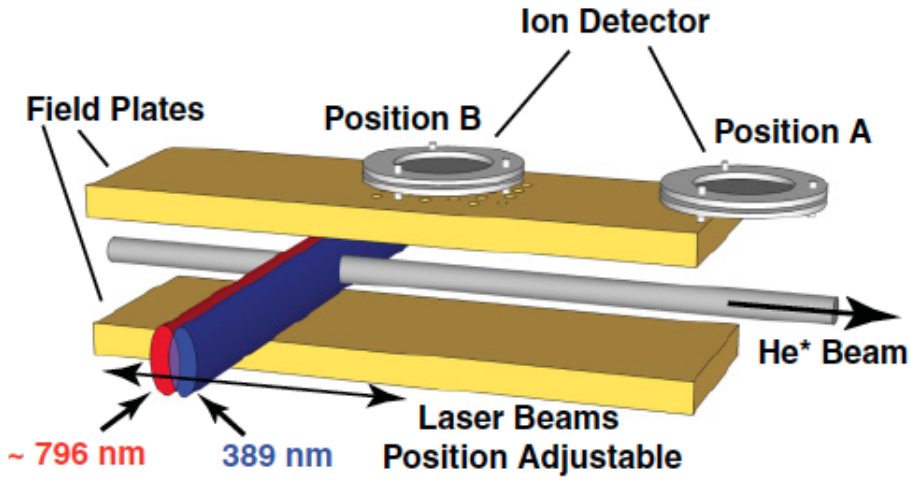

Figure 5.2: Ion detector scheme [12]. The detector sits on the top plate or is placed on the edge. Either way it can only collect the ion signal directly from right below its position when there is even a very small field on.

takes for them to reach the plate and collide with it is incredibly short. For example, for a field as low as 1 V/cm, the time it takes for the ion to reach the plate is roughly 1.6 μs, and accordingly it can only travel $\sim$ 1.7 mm horizontally during this time with the atomic beam velocity of $\sim$1 km/s.

The position of the blue and red laser beams can be changed. As they are reflected by mirrors on the same translation stage in front of the window on the interaction chamber and the blue laser is on another small stage mounted on the translation stage that can be adjusted separately. This way by moving the big translation stage, we can move the two laser beams at the same time without worrying about the relative position change whereas by moving the small stage, we can just adjust the position of the blue laser without moving the red laser and change the overlapping area of the two laser beams. The STIRAP efficiency

can be maximized by tuning the overlap as we introduce in Chapter 4.

A high voltage power supply feeds the electrodes of the ion detector to attract ions to hit the MCPs. The ions going into the ion detector, as we already introduced in Chapter 2, will be amplified twice by MCPs through secondary emissions. The signal being collected by the anode can be either fed to a display circuit (a current amplifier and an oscilloscope) or a counting circuit (a pre-amplifier, an amplifier and a pulse counter). We can obtain the ion flux rate though either way and calculate ionization rate based on the data. From here we will mainly use Xiaoxu Lu's data in her thesis as a discussion [11].

We can first skip the current amplifier and send the output of the anode directly to the oscilloscope in the display circuit. During this process the ion detector was located at A which means there is a distance between the STIRAP region and ion detector position. This data set is collected with a distance of 35 mm. We could see single pulses of 5 ns width and 3.5 mV height [12] with field intensity of zero. We can calculate the MCP gain and check if it matches the label from the manufacturer. We see with a 50 Ω coupling in the circuit, the total gain of the two MCPs is

$$G_{total} = \frac{\frac{3.5mV}{50\Omega} \times 5ns}{e} \approx 2.2 \times 10^6 \tag{5.5}$$

This result matches the labeled value provided by Photonis, Inc. When we take the current amplifier (1.25 MΩ) into account, typical signal (data from Xiaoxu Lu [11]) height is 1 V for the 24S state. This leads to an absolute

current of 40 nA, and the ion counts could be calculated as

$$\frac{40\text{nA}}{(2.2\times10^{6})\times(1.6\times10^{-19}\text{Coulomb})}\approx 1.1\times10^{5}\text{count/s} \tag{5.6}$$

In the Rydberg detection process, figure 5.3 below shows typical reading on the oscilloscope in the display circuit [12]. We scan the electric field and keep the red laser frequency fixed in this measurement.

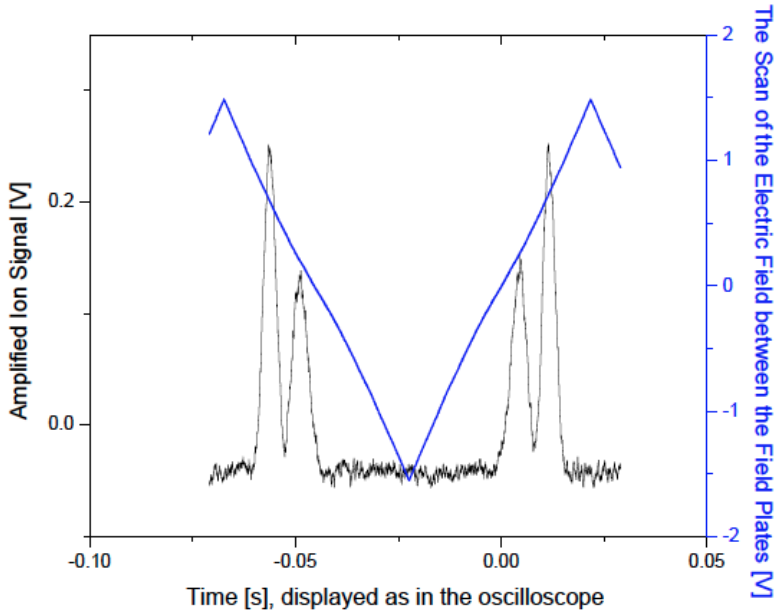

Figure 5.3: Typical ion detector reading during the STIRAP excitation of helium atoms [48]. The blue line shows the scan of the field intensity is on the order of 2 V. We see there are two peaks, showing this is a non-zero angular momentum $l \neq 0$ state. There are two Stark manifolds in the sweeping range. There will only be one peak if it is an S-state with $l = 0$.

With the knowledge of a single ion generates a pulse of 5 ns, we can send the output to the counting circuit. The signal from the ion detector is first

sent to a PRE Amp (ORTEC mode 113) and a multimode amplifier (ORTEC mode 410) then to a 50 MHz counter (HP 5302A) to directly count the pulse rate. This result well matches what we obtained from the display circuit which is $\sim 1.1 \times 10^5$ count/s for the 24S state [11]. The rates for different states may vary a bit but in general, they match the estimated values pretty well.

Rydberg atoms are very likely to decay in the path as it flies in the system. As we showed in the last section, the ionization rate is pretty low compared to the decay rate. So the ion signal output here (the field plates are grounded so all the ions created by the BBR will not fly towards the field plate and can be detected) is only small part of the total ion signal flux. Through a decay rate experiment we can estimate the decay rate of Rydberg atoms and figure out the decay correction and calculate the real ion flux measurement. From the decay curve of the 24S state we can get the after-correction ion flux rate should be $\sim 6.7 \times 10^5$ count/s. This means only 15% of the ion flux is detected by the detector after decay. Consider that the total metastable helium flux is $3{\times}10^8$ count/s and the STIRAP efficiency is between 30% to 50%, we can see the ionization rate here is roughly 0.6%.

So far we set up a Rydberg detection system using ion detector, figure 5.4 shows a typical measurement of the STIRAP ion signals. This is taken while we try to find the relative overlapping area to maximize the STIRAP efficiency.

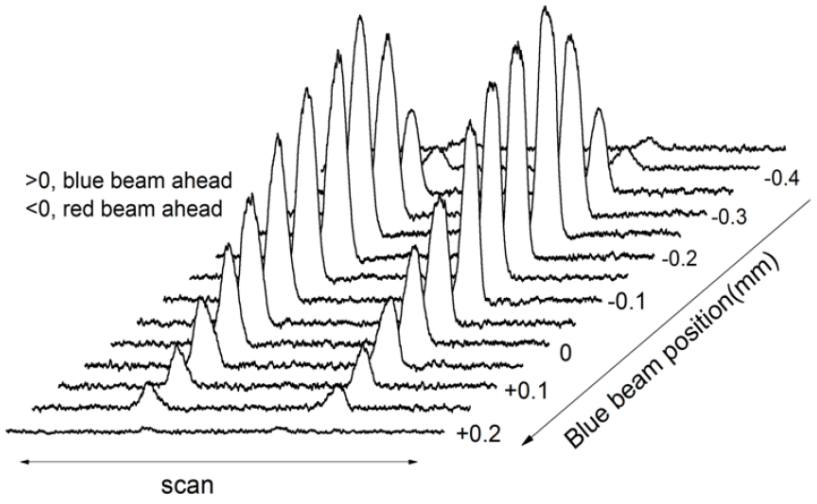

Figure 5.4: Typical measurement of the STIRAP ion signal as the overlap area varies [11]. We can see that when the blue laser is ahead by 0.25 mm the signal is maximized.

5.4.2 Field Ionization

To determine the source of ionization in our system, field ionization is measured and compared with the BBR ionization. We know for field ionization, atoms only get ionized when the field intensity is above threshold and provides more energy than the ionization energy. Classical field ionization threshold is given by $5 \times 10^9/(16n^4)$ V/cm. For example, for the n=24 states, this threshold is around 900 V/cm [35].

As we mentioned above, field ionization has to be carried on with the detector position at position B in figure 5.2. Because the field ionization is so strong that with the electric field beyond threshold, no Rydberg atoms will reach position A without being ionized, and the ions will immediately collide with the field

plate so we can not see any signal output from the ion detector.

By letting the ion detector sit on the holes at position B right above the STIRAP region, Rydberg atoms get ionized once they are created and they can be immediately collected by the ion detector. When the laser beams are directly under one of the holes, we can see a strong ion signal from the oscilloscope. This signal is far greater than the BBR induced ion signal. Notice here that the laser beams are well regulated so the widths of the beams are both shorter than the diameter of the holes. But when we move the overlapping laser beams a bit, even a small distance, say $\sim$0.5 mm, the signal would vanish. This means pretty much all Rydberg atoms get ionized immediately and collide with the plate as ions, leaving no signal for the detector to detect. This proves again that the ions can barely travel horizontally when there is a field. Further more, for field ionization, the STIRAP efficiency is usually low because we are on the continuum Stark Map with a strong external field.

We can compare the ionization rate of field ionization with the BBR ionization rate. It turns out the rate of field ionization is usually 20 times higher [11] which explains why the field ionization signal is stronger even with the lower STIRAP efficiency. Through this we see that the BBR can ionize only a small part of the total Rydberg atoms, leaving enough Rydberg atoms behind to be ionized and detected. So it makes sense to put the detector at A and move the laser beams for decay rate measurement (the field plates are grounded here, of course).

We can lower the field intensity and monitor the ion signal as we keep the

laser beams under one of the holes. We can see once the field goes below the threshold, the signal would drop down to a distinct low level. The ion signal now is produced by the BBR ionization or other potential sources. We still need to verify the exact mechanism but right now we know by lowering the intensity to the threshold and moving the laser beams, we can map the holes on the board. Several groups of measurements with different n values were done [11]. The ionization thresholds for different n are: 2930 V/cm for n=18; 940 V/cm for n=30; 25 V/cm for n=60. These results matches well with the classical ionization limit, $5 \times 10^9/16n^4$ V/cm. [35] The field intensity we usually use is way below the ionization threshold, so we can confirm that the ions from the system are not produced by field ionization. This result corroborates Rydberg spectroscopic measurements because now the states could be identified by their field ionization threshold.

5.4.3 Testing Blackbody Radiation Ionization by Varying Temperature

As in Planck's law equation 5.1, the blackbody radiation power scales with temperature. So we can double test the mechanism by varying the temperature of the interaction region and measure the ion signal and study the trend. This is done by heating up the field plates. In Chapter 2 we mentioned that there are four power resistors (each with power of 25 W) attached to the field plates for heat generation. By changing the current going through the resistors with good thermal contact, the temperature in the interaction region can be changed

at our will. A thermocouple is deployed to measure the temperature. It is attached to one of the resistors. The thermocouple uses Nickel-Chromium and Nickel Aluminum as the electrodes. The real temperature is proportional to the voltage across the thermocouple. The voltage and temperature correspond to each other as -0.023 mV at 0 °C and 2.27 mV at 100 °C [11].

As we increase the temperature, the BBR intensity should respond and increase, too, causing more ionization and we should be able to detect stronger signals here. Figure 5.5 shows the relation of ion signal strength and temperature of the plates.

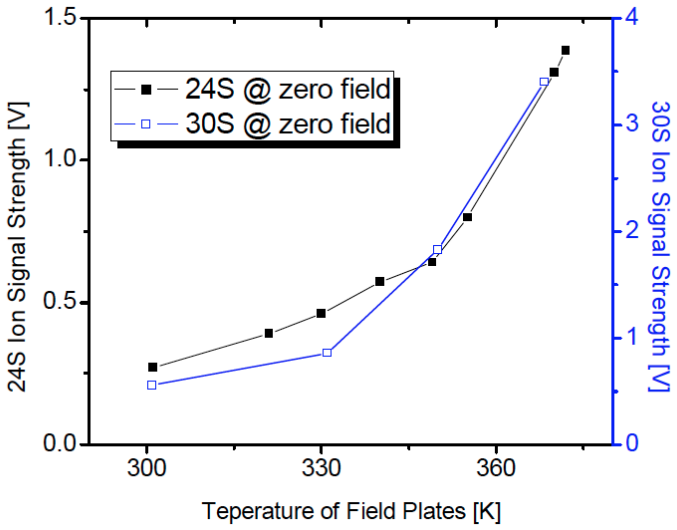

Figure 5.5: Ion signal strength versus temperature for 24S state and 30S state. The field intensity is zero here so S-states are measured, so there will not be any field plates attracting ions and mess with our measurement [12].

From what figure 5.5 shows, the ion signal increases significantly as we heat the plate. This result well supports the theory of the BBR is the source of

ionization in our system.

5.4.4 Collisional Ionization

There is enough evidence so far to prove that field ionization is not the source of ions in our system with the field staying below several hundred volts just for the Stark tuning use. But there could be one more possible origin of ionization other than the BBR: The collisional ionization. When two Rydberg atoms are sitting close, one atom's electron can likely drop to a more deeply bound level as the other atom gets ionized [50]. For the metastable helium atoms, they carry very high internal energy which is higher than the ionization energy limit of Rydberg helium atoms and not to mention Rydberg atoms. So if the atoms collide with each other theoretically it is quite possible to produce ionization. This process is known as Penning Ionization which is a form of chemi-ionization. We don't know if this ionization happens in the STIRAP experiment so we need a method to check it.

The probability for atoms to collide into each other depends on the mean atomic spacing, which means spatial density of the atoms. This does not equal to the absolute pressure because ground state atoms make up a good portion of the beam flux. If we change the density in the interaction region the relative ionization rate is not responding to that, we can rule Penning Ionization out of the system.

Figure 5.6 and figure 5.7 below are a group of measurements of the particle count with different flow pressures and source voltages [11]. It is easy to un-

derstand why we choose these two parameters as variables. When we increase the source current, the source excites more ground state atoms to state $|1\rangle$, the metastable state, creating more atoms with the capability of ionizing Rydberg atoms via Penning Ionization. When we change the flow pressure of the helium, we make more atoms (ground state, metastable state... everything) in the space. If there is collisional ionization in the process, theoretically there should be a higher probability of collision giving that the STIRAP efficiency and metastable production rate stay the same. The SSD signals in figure 5.6 and figure 5.7 come from the SSD detector mentioned in Chapter 2, after using the 1083 nm laser to deflect the remaining metastable atoms. These readings are a good reference of the particle counts.

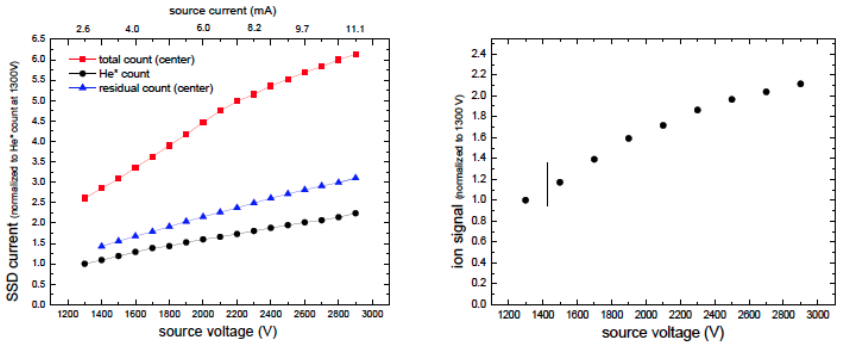

Figure 5.6: By adjusting the source current to manipulate the density of metastable helium [11], we can see that the resulting signal is basically linear to source voltage. So the ionization rate is independent of metastable helium density in this experiment.

From figure 5.6 above with source voltage being scanned from 1300 V to 2900 V, we can see that the signal is almost proportional to source voltage. The ion signal divided by metastable helium count can be treated as relative ionization

rate. That tells us that the ionization rate almost stays the same with these different source voltages. The reason for a higher ion signal is that we simply have more metastable atoms to create more Rydberg atoms with unchanged STIRAP efficiency. Here we can basically confirm that in this experiment, neither metastable-Rydberg nor Rydberg-Rydberg collision creates ionization because the rate does not change with the density of metastable atoms. And the UV photons brought along with metastable atoms does not change the ionization rate, either. We can also vary the flow pressure to check the relation between ion signal and flow density. Figure 5.7 below shows the relation between ion signals and pressure. With higher source flow pressure, more ground state helium and less metastable atoms get to the interaction region. As the pressure is increasing, the STIRAP efficiency stays constant and the only parameter that increases with the flow pressure is the pressure in the chamber. As the source outlet pressure goes from 2 Torr to 4 Torr, the ion signal decreases as the metastable atom counts decrease.

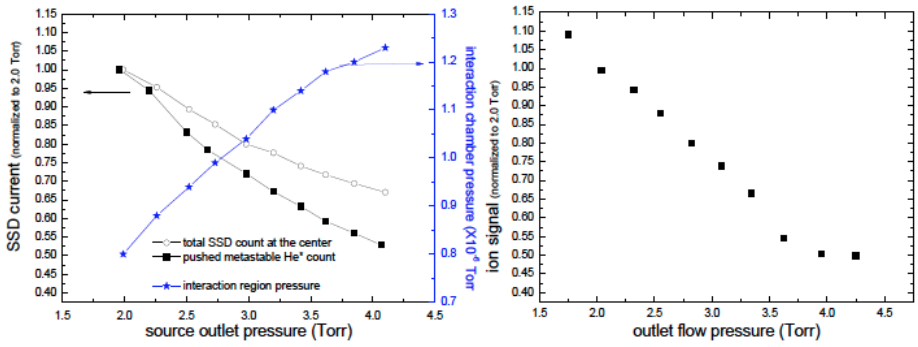

Figure 5.7: Signals picked up by the ion detector as we change the source pressure [11].

So far we have not figured out a good explanation why the collisional ionization is not happening in the interaction region, but we certainly prove that it won't be a factor that affects the ion signal. For if it was, the ionization rate would increase with the metastable atom density.

5.5 Decay Rate Measurement

Due to radiative emission, Rydberg atoms created from the STIRAP will decay as they travel to the ion detector. To measure the decay rate, we can place the ion detector at position A with different laser beams positions. Figure 5.1 shows the data of rates of nP series and here we will use them as an example. In this measurement, the relative distance between the laser beams—the overlap does not change to maintain the local maximum STIRAP efficiency at each position and the ion signal corresponding to laser beams at different longitudinal positions are measured. The field plates are grounded at this time so the generated ions won't be attracted to the field plate and the ion signal of them can be measured by the detector.

The ion signals decrease as the interaction region is moved away from the detector, as we expect. The decay curve well fits to an exponential function. The decay signals of 24S and 30S are measured to demonstrate this, as in figure 5.8 and figure 5.9.

The calculation based on data above shows that the characteristic travel distance for 24S state is 17.6 mm and corresponds to a Rydberg life time of 16.4

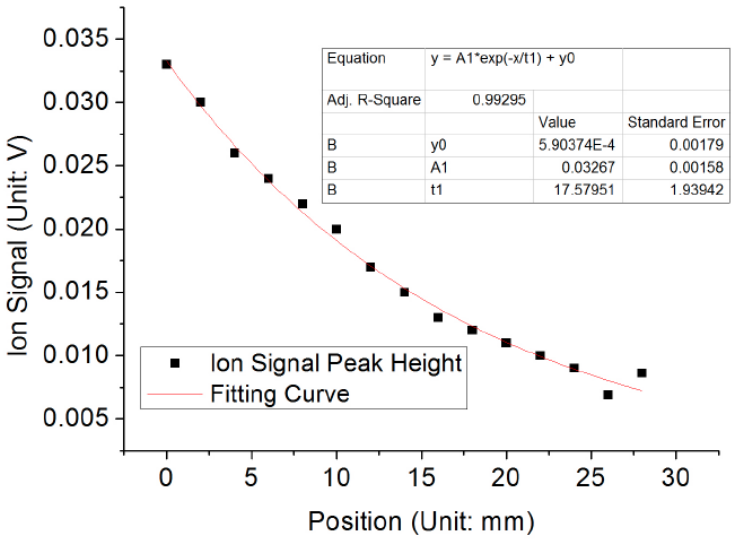

Figure 5.8: Ion signals at positions of different distance to the interaction position for $n = 24$ [12].

μs [11].

It's similar for 30S state. The ion signal appears to be an exponentially decaying trend the average "decay time" of 20.1 μs [11] as figure 5.9 shows.

The derived Rydberg life time from the measurement above is actually a little longer than its theoretical value. This is because the depopulation process we mentioned above competes with spontaneous decay. For the target states that the original Rydberg atoms diffuse into, they have higher ionization rates and will ultimately contribute to the ionization process. Making the observed ion signal decay slower. In all, the data shows that the ionization rate by the BBR is much faster than radiative decay rate. Considering that the direct ionization rate given in figure 5.1 is so low, and from the depopulation theory, we may infer that multiple ionization processes exist in the experiment.

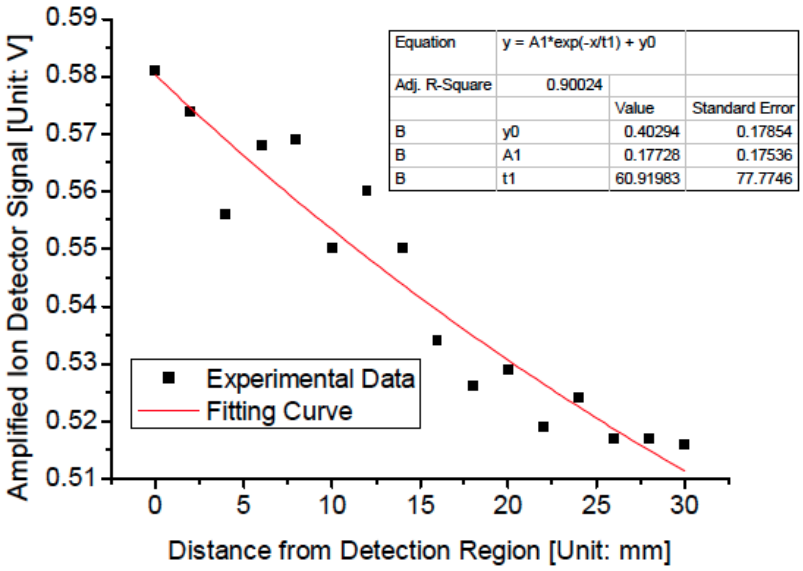

Figure 5.9: Decay curve of 30S state with distance between the interaction region and the ion detector being changed [12].

5.6 Ionization Rate

As we mentioned above, the BBR does not only produce the direct ionization of Rydberg atoms but also transitions into neighboring states. The direct transition rates shown in the table below are from Dr. Glukhov [48]. According to Glukhov's calculation the direct BBR induced ionization rate for 24S state should be ∼300 count/s. That means during the time period of 15 μs for the atomic beam to travel through the interaction region, about 0.45% of Rydberg atoms are ionized [11]. Similarly for 24D state, this percentage is 2.3%. The numbers and datum are from Glukhov et al. [48] and taken to be used as a demonstration here. Credits to Xiaoxu Lu and I. L. Glukhov.

n	24S - nP transition rates (count/s)	nP ionization rates (count/s)
20	1127.8	1386.5
21	1726.2	1410,7
22	3135.2	1420.6
23	9337.2	1419.0
24	3762.4	1408.3
25	142.6	1370.3
26	133.4	1366.8
27	101.7	1339.2
28	78.1	1308.5
29	61.4	1275.7

Table 5.1: Trasition rates for 24S to nP states and nP ionization rates (T=300K) [11].

As Rydberg atoms are redistributed to states with higher ionization rates, multiple step ionizations other than the direct ionization process happen. For example, a 24S state can first transit into an nP state, then get ionized, and we have to take all possible n values into account to calculate the actual ionization rate. Rates for the atoms to transit from 24S to nP states (n from 20 to 29) are shown in the table 5.1. Adding all possible paths with in the traveling time of 15μs, the total two-step ionization rate is roughly 0.62%, and this rate for 24D is 0.1%. The ionization that takes three or more steps does not contribute significantly to the total ionization rate. So we have a total ionization rate of 1.07% for 24S state and 2.4% for 24D state. This would explain why the ion signal of the Stark manifold is usually much more stronger than the rates of the S states even though they may have the same STIRAP efficiency [11].

Since Penning Ionization, field ionization, and three or above steps ionization are ruled out in our experiment, the conclusion can be drawn that the ion signal during the STIRAP experiment is mainly produced by the BBR radiation within

two steps.

5.7 Rydberg Spectroscopy

Based on the ion signals detected by the ion detector, we are able to map the Rydberg-Stark Spectroscopy of helium Rydberg atoms (data from Xiaoxu Lu [11]). The electric field is scanned from zero to 170 V/cm (of course this range is under the ionization threshold) to sweep across different Stark states. It is also an option to choose to scan the red laser frequency and fix the electric field, and the red laser frequency is fixed here at four different values. As it is shown in figure 5.10 [11].

In figure 5.10, the blue dots mean the experimental results that there is an actual Rydberg atom state at certain energy level at the corresponding electric field intensity. When we observe a peak on the oscilloscope from the ion detector, it indicates that there is an ion signal generated from Rydberg atoms as the electric field is being scanned. It does not matter what the peak size and peak width are like because they are not concerned with the Stark effect. The only information we are interested in is the peak position. The splitting dashed lines are theoretical calculations done by Prof. T. Bergeman of the Stark map of n=24 Rydberg atoms, which the experimental data matches amazingly.

There should always be a small error bar (on the map it is smaller than the data dots) in our measurement, typically within 2%. The main reason other than equipment errors causing this is the Doppler broadening induced by

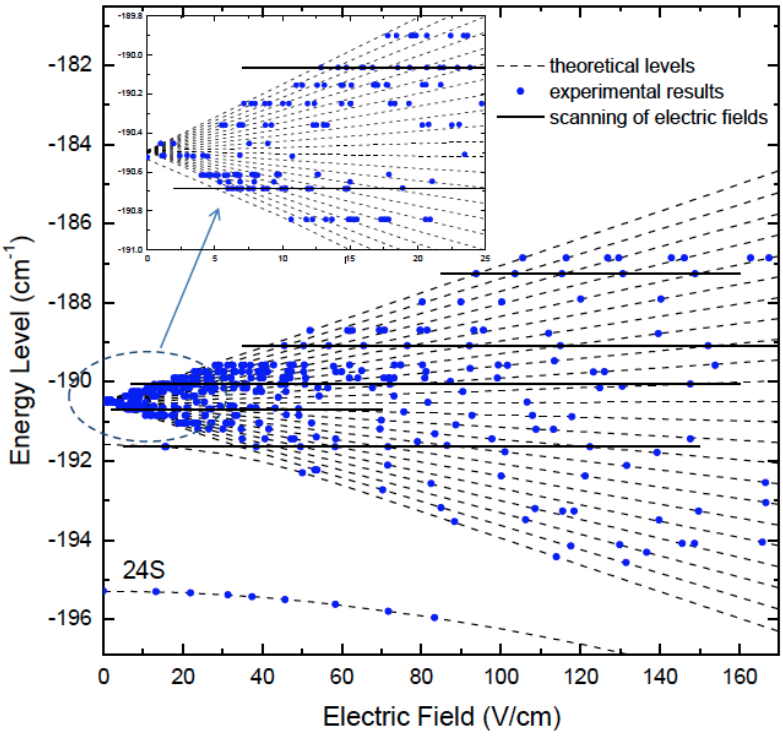

Figure 5.10: Rydberg-Stark map of the n=24 S states and manifold states with different l values. The blue dots are experimental results by Xiaoxu Lu and Yuan Sun [11] [12], and the dashed lines are theoretical calculated Stark Map made by Prof. T. Bergeman, and the solid lines indicate the electric field scannings.

transverse velocity spread of the atomic beam. Atoms with different transverse velocities see different laser frequencies in the STIRAP system, causing a frequency detuning in the STIRAP experiment. So far this is the main obstacle in the way of achieving a higher STIRAP efficiency. The only tools in the system that we use to limit the atomic beam spread angle is a 1 mm nozzle and a 3 mm aperture on the skimmer plate as we introduced in Chapter 2. In the low field area there would be some earth's magnetic field interfering with the signal. To sum up, the error bar won't be a big problem in this measurement.

Chapter 6

Absolute STIRAP Efficiency Measurement and 1083 nm Force

6.1 Introduction

In Chapter 5, we have seen that using the ion signal is an efficient way to detect Rydberg atoms. But that does not give us the absolute measurement of the STIRAP efficiency. For it can not directly provide the number of Rydberg atoms nor metastable atoms (the ion signal does increase with Rydberg atoms count but we can not confirm that they are proportional to each other). We still need a method to obtain the absolute Rydberg atoms count and to do that,

we first have to distinguish metastable atoms and the Rydberg atoms. This is done by using the 1083 nm laser downstream of the interaction region to excite the metastable helium to another state 2^3P_2 state and thus a momentum is transferred to the metastable atoms in the beam, but there won't be any spatial impact on the Rydberg atoms. The separate signals are picked up by the SSD detector at different transverse positions as we already introduced. We can always monitor the signal change with or without the STIRAP red and blue lasers or the 1083 nm laser and obtain the deflection ratio and calculate the absolute efficiency.

6.2 Experimental Setup

Figure 6.1 shows a brief scheme of the absolute efficiency measurement setup. The 1083 nm laser nowadays replaced the old laser which used radiation pressure to deflect the residual metastable helium atoms, because the bichromatic force is much more stronger than radiative force (see discussion in next section) and provides a more complete separation between the metastable atoms and the Rydberg atoms.

The STIRAP lasers will partially overlap and drive the metastable atoms to the Rydberg state, as we discussed in Chapter 4. This happens in the middle of the field plates whose field intensity is tunable. The distance between the metastable helium source and the interaction region is around 26 cm. The beam coming through the interaction region should consist of Rydberg atoms,

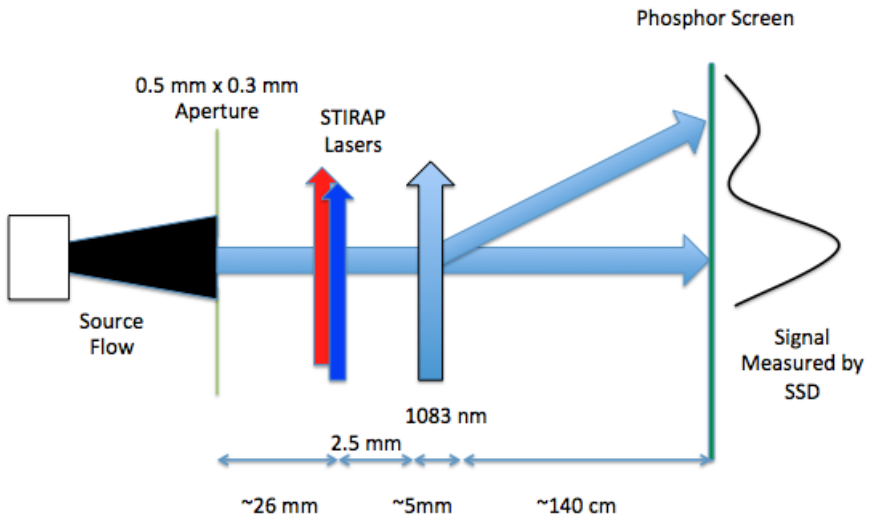

Figure 6.1: Experimental scheme of the STIRAP efficiency measurement. The SSD detector in the down stream collects signal at different transverse positions.

metastable atoms, residual ground state helium atoms and UV photons. The UV photons won't be a big factor because of their low count. The 1083 nm laser comes right after (usually about 2.5 mm as the position of the STIRAP lasers can be changed) the two STIRAP lasers and produces bichromatic force to spatially deflect the metastable atoms. There is a mirror to retro-reflect the 1083 nm laser to create standing waves of π pulses and a phase delay. The 1083 nm bichromatic beam is 5 mm wide along the beam direction.

About 1.4 m downstream there is the detection region. We expect the metastable atoms, after deflection, would transversely travel about 4.5 mm away (as the SSD detector detects a new peak there) during the time it takes for the beam to reach the detection region [11], and this signal strength is confirmed

proportional to the metastable atom counts. Now with the atoms separated from each other, we can calculate the absolute efficiency.

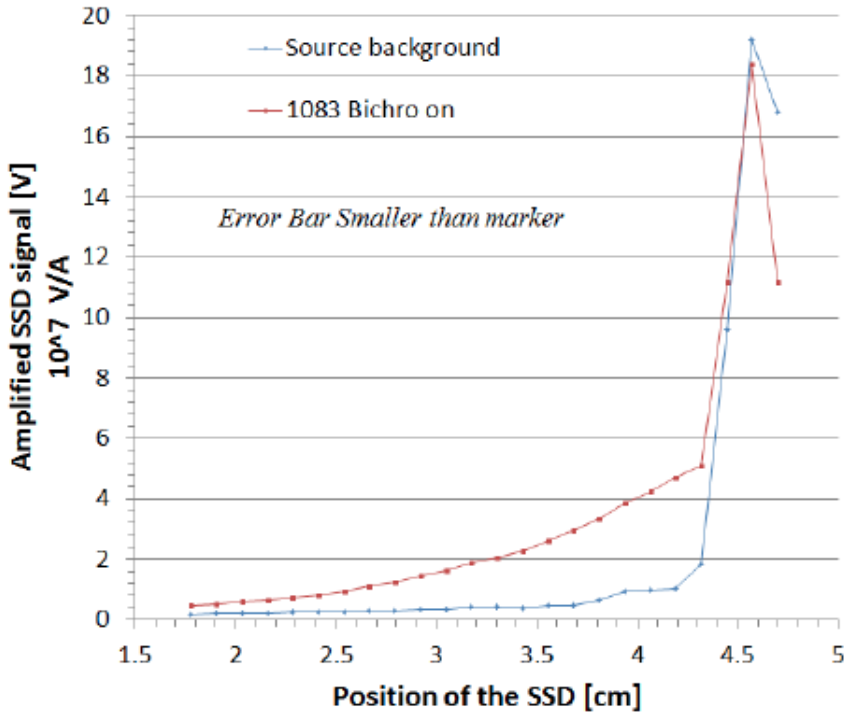

Figure 6.2: Atomic profile measured at different transverse SSD positions [12]. We see that with the 1083 nm bichromatic beam on, the atom transverse distribution is changed a bit. The metastable atoms get pushed to the zero position.

6.3 Bichromatic Force

The bichromatic force itself has been studied as an individual subject in our lab [51] [38]. In our experiment, the 1083 nm bichromatic laser comes from the adjacent lab as we are using a flip mirror to send it into our lab through a polarization maintaining fiber. After two amplification stages (as in Chapter

3) it is ready for our experimental use. The basic idea is to use two counter propagating π pulse beams with the same frequency to generate momentum "kicks". The waves are set to have a phase difference and this way one beam will induce absorption and the other will induce stimulated emission later. We will briefly describe this process here and discuss the reason of the bichromatic light behavior and why it is used to replace the old radiative force setup.

We first start with π pulse model which provides a basic idea of the whole picture. In a two state Rabi problem, a pulse on resonance with the atom that drives it to the excited state, causing the system state vector to rotate 180°, or π, in a period of time is known as a π pulse. From Chapter 3 we know the 1083 nm beam has two frequency components ($\omega \pm \delta$). Here the carrier frequency ω is just the resonance frequency between states 2^3S_1 and 2^3P_2. These two components are of equal strength and we see they have symmetric detunings above and below resonance frequency. Here the total laser field can be expressed as

$$\begin{aligned} E &= E_0 \cos\left[(k+\Delta k)z - (\omega+\delta)t\right] + E_0 \cos\left[(k-\Delta k) - (\omega-\delta)t\right] \qquad (6.1) \\ &= 2E_0 \cos\left(kz - \omega t\right) \cos\left(\delta t - \Delta k z\right) \end{aligned}$$

where z mm is initial position. $k = \omega/c$, $\Delta k = \delta/c$.

This way the beam can be described as an amplitude modulated wave with the carrier frequency at ω and modulation frequency of δ, a series of pulse chains.

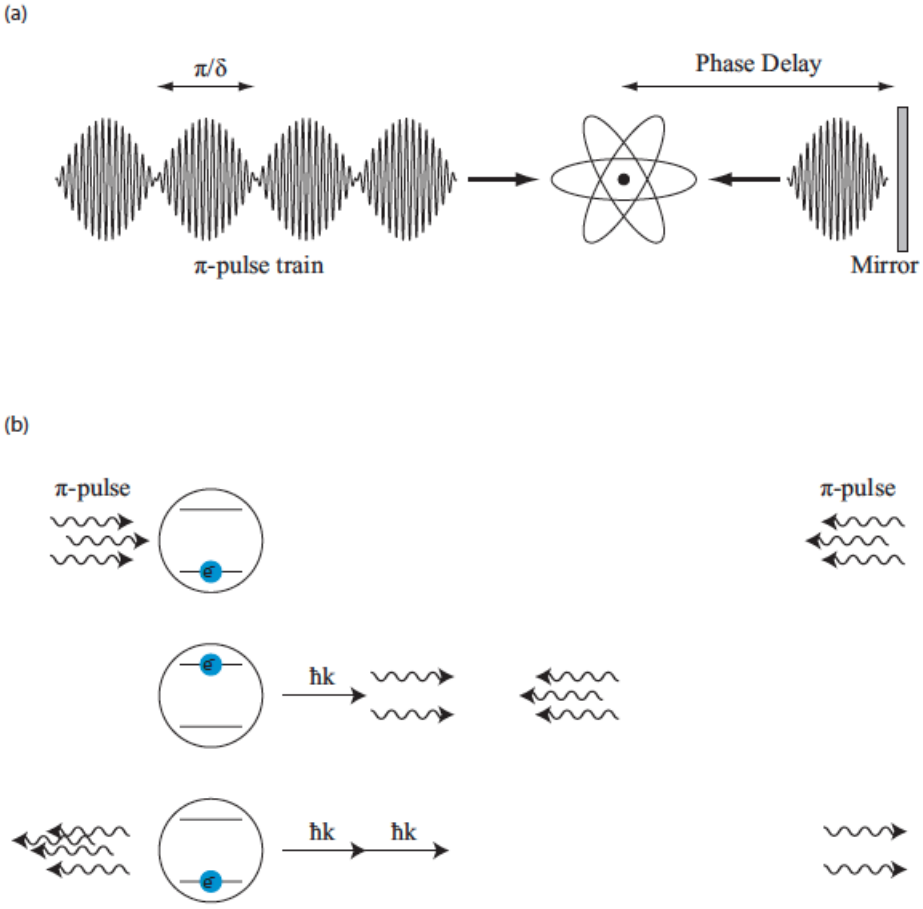

Figure 6.3: Bichromatic force demonstration [12].

If the intensity of the beam, which has control over Rabi frequency, can be set that the π pulse condition is satisfied [52], as $\Omega = \frac{4}{\pi}\delta$, we may guarantee a complete photon transition, an energy level exchange, in one modulation period [11] with one π pulse.

This is a one dimensional problem and we can reflect the beam onto its own path and create standing waves. Figure 6.3 is a brief demonstration of this mechanism where we set the π pulse is traveling right and is getting reflected to the left. Now here comes the interesting part. We can always set the distance between the atomic beam and the reflection mirror, creating a path difference hence a phase delay between the pulses from left and right interacting with the atom. This way when the pulses travel through the atom and interact with it, the atomic wave function will always be in phase with the pulse coming from one direction and out of phase with the other. As in figure 6.3 (b), the atom absorbs a photon from the wave traveling from the left and gets to the excited state without absorbing photons from the right. In this process the atom gets a "kick" and gains a momentum of $\hbar k$ to the right. The excited state atom, under the presence of the right wave, will go through a stimulated emission process and then emits a photon to the left hence it gains a momentum of $\hbar k$ again to the right (where as in spontaneous emission the atom emits photon to a random direction)! This way the atom will gain two "kicks" in one pulse period. As the next pulse from the left arrives, this process goes again, and over again as the pulses keep coming, pushing the atoms to the right.

And we can quantitatively calculate the force. Since one π pulse provides a

momentum in time period of π/δ, the resulting force is momentum by time:

$$F = \frac{P}{t} = \frac{2k\hbar\delta}{\pi} \tag{6.2}$$

One thing to be noted is that the bichromatic force does not rely upon the spontaneous emission as the radiative decay rate γ is so small compared to the bichromatic detuning δ. Even without the spontaneous emission to scatter the power, the stimulated emission can still take place here and provide a force. The result above is the ideal case where we ignored the spontaneous emission. From here we take it into account and the total force is reduced by a factor of 2 [53], and we have that the bichromatic force of $\hbar k\delta/\pi$ which could be much stronger than the radiative force $\sim \hbar k\gamma/2$.

In our setup, the light output will first go through a spherical telescope and get focused. The position of the reflecting mirror which creates standing waves is about 625 mm [11] from the atomic beam. This gives us a path difference of twice the distance $2d = 1.25$ m, corresponding to a phase delay of $\pi/2$. The 1083 nm laser has to pass a quarter wave plate to get circularly polarized if the STIRAP is set to $\Delta m = \pm 1$ and match the polarization.

It is recommended to use the laser with power a little higher than the theoretical value to avoid losses due to the imperfection of equipment alignments. In this case the intensity of 1083 nm laser is $5000 s_0$ and s_0 is the saturation intensity [11] and here the force is still a little lower than the anticipated value. It is good enough for the experiment, though. A broader-than-the-actual signal

peak is expected because of the longitudinal velocity spread of the atoms as we introduced in the time of flight section. As figure 6.2 shows, the bichromatic laser deflects the metastable atoms to a different transverse position. We can measure the signal difference with the 1083 nm laser on or off to calculate the efficiency. Figure 6.4 shows a good demonstration of typical reading of efficiency measurement using the SSD detector.

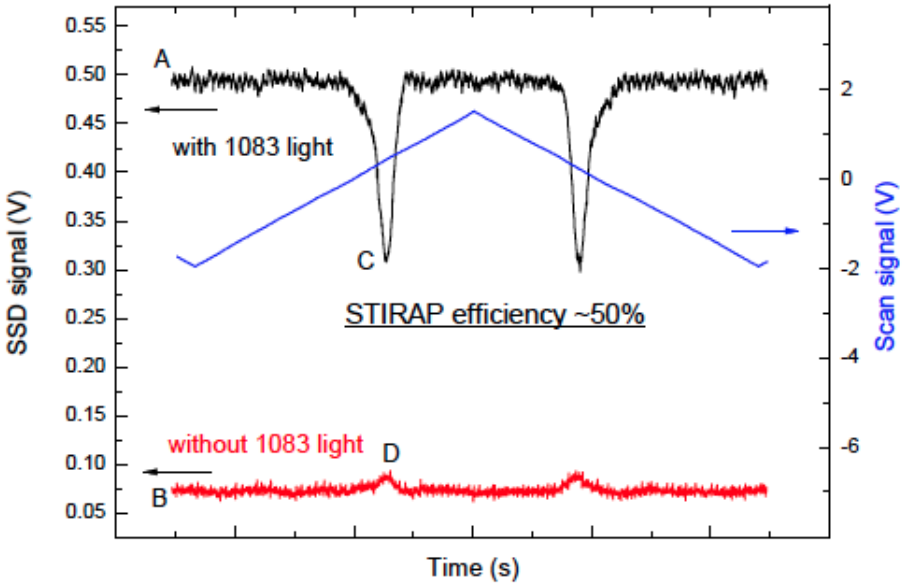

Figure 6.4: Typical signals of STIRAP efficiency [12]. The folded line shows the scanning electric field, corresponding to the volts value on the right. The signal above is the SSD signal with 1083 nm light on and the bottom is signal with the 1083 nm light off.

As we see, when the electric field gets to the right value on the Stark map, there will be Rydberg atoms being generated that do not experience the push from 1083 nm laser and further collected by the SSD detector. We see in the scan range there are two dips of the top signal with 1083 nm laser on. These

two dips corresponds to the same Rydberg state on the Stark map as the field is being scanned back and forth. The dips show that there are Rydberg atoms being generated as the data is being taken at the expected metastable atoms' deflection position. If there is no Rydberg atom at all, we should see two flat lines with minor fluctuations. If the STIRAP efficiency ideally gets to 100%, we can see the dips get all the way down to reach the bottom signal. There may be two small peaks on the bottom signal at position D and its mirror image position about the scanning, and this may be because of the expansion of the Rydberg beam as they pass the electric field. Here we can calculate the efficiency: $Eff = (A - C + D - B)/(A - B)$. When there are no peaks on the background signal, we could simplify it to $(A - C)/(A - B)$. In the case of figure 6.4, the dip signal is around 0.2 V, as the total signal is around 0.4 V. So the STIRAP efficiency here is around 50%, and is by far the highest one could get with current apparatus with various parameters [11] as we are about to introduce. Efficiency of different Rydberg states were also measured but no data has gone above this value. It is fairly surprising that according to the STIRAP theory in Chapter 4, ideally we can push the efficiency as high as 100%. We will discuss the reason in the last section of this chapter.

6.4 STIRAP Efficiency with Different Parameters

With 1083 nm laser introduced into the system, we are ready to measure the absolute efficiency of the STIRAP process. There could be many reasons affecting it. The laser parameters, source parameters, intermediate states, etc. Different states have different requirements for certain parameters to achieve the highest STIRAP efficiency. Here we'll use results from previous experiments [11] [12] as a sample to present the conclusions so far. For this discussion, only the $n = 24$ states are considered here, because the laser power which determines Rabi frequency needed by $n = 24$ state (to get the best efficiency) is under the limit that our laser system can provide.

Efficiency data from different laser beam positions are adjusted to have the overlapping ratio with the highest signal to provide local efficiency data. In these measurements we have to take the radiative decay of the Rydberg state atoms in account and make a correction as the decay path varies.

6.4.1 Rabi Frequency and Laser Intensities

As are introduced in Chapter 4, Rabi frequencies are to be controlled to get to the adiabatic state. They can be derived from $\Omega = -\frac{e}{\hbar}\varepsilon_0\langle e|r|g\rangle$ which is related to light intensities $\Omega = \frac{\mu}{\hbar}\sqrt{\frac{2I}{\varepsilon_0 c}}$. μ is the transition moment and can be expressed as $e\langle e|r|g\rangle$. Table 6.1 shows the conversion of the Rabi frequencies of corresponding transition between states to pump and Stokes laser intensities. It

is done through the calculation of the matrix elements of selected transitions.

Transitions	$2^3S_1 \rightarrow 3^3P_2$	$3^3P_2 \rightarrow 24^3S_1$
Δm=0	$\Omega_P(t) = 14.9 \times \sqrt{I_P(t)}MHz$	$\Omega_S(t) = 1.67 \times \sqrt{I_S(t)}MHz$
$\Delta m = \pm 1$	$\Omega_P(t) = 12.9 \times \sqrt{I_P(t)}MHz$	$\Omega_S(t) = 1.45 \times \sqrt{I_S(t)}MHz$

Table 6.1: Conversion from light intensity (W/cm^2) to Rabi frequencies of STIRAP to n=24 S states [11].

This table shows the conversions of Rabi frequency to laser power. We can see from the table that the Stokes lasers' Rabi frequencies are relatively smaller than the pump lasers' because of the weaker transition strength. We already introduced that in Chapter 1. So to produce comparable Rabi frequencies, we have to adjust the laser powers correspondingly.

With table 6.1 we can convert the Rabi frequency to laser power required. The STIRAP beam size is set with intensity FWHM of horizontally 0.5 mm and vertically 2 mm. From the table we see to get comparable Rabi frequencies, the red laser intensity has to be two orders above the blue laser intensity. To get a peak Rabi frequency of around 15 MHz, the blue power output of 15 mW and red output of 1 W is needed. This rings a bell for us that when choosing the target states we have to be careful of the upper limit of the power output of our laser system. The magnetic quantum number change Δm value in the table indicates the "path" that the transition process takes. As from the selection rules a transition can only have $\Delta m = 0$ or $\Delta m = \pm 1$. Linearly polarized lasers drive transitions of $\Delta m = 0$ and circularly polarized lasers drive transitions of $\Delta m = \pm 1$. Since the relation between Ω and I of $\Delta m = 0$ and $\Delta m = \pm 1$ do not differ that much, we will just take the weighted average to calculate the Rabi

frequency of them.

6.4.2 STIRAP Efficiency of n=24 States with Different Laser Parameters

We may vary the laser intensities to monitor the STIRAP efficiency change. The best power we can provide with our apparatus is up to 60 mW of blue laser and $\sim$ 1W of red laser in the interaction region. This means the blue laser is tending to cause the efficiency more saturated.

Here we use Xiaoxu Lu's [11] data as a demonstration to see how the STIRAP efficiency changes with blue and red power. We take blue power at 55 mW and 5.5 mW with different red power and measure the absolute STIRAP efficiency.

The two dotted lines indicate the STIRAP efficiency with different red and blue power. As we see the STIRAP efficiency first rises fast as it is reaching the saturated value in figure 6.5. We can see the efficiency is more saturated with respect of blue laser. The highest efficiency point in figure 6.5 is of 55 mW blue light and 700 mW red light here. As the blue laser power drops from 55 mW to 5.5 mW with the same 700 mW red light, the efficiency drops from 42.5% to 28%; If the red laser power drops from 700 mW to 70 mW with the same blue light power, the efficiency drops to about 11%. We can not provide more laser power but that is not the reason higher efficiency can not be achieved as the trend of the curves shows, it is unlikely that the overall efficiency will go beyond 50%.

We can also compare the STIRAP efficiency of $n = 24$ manifolds states with

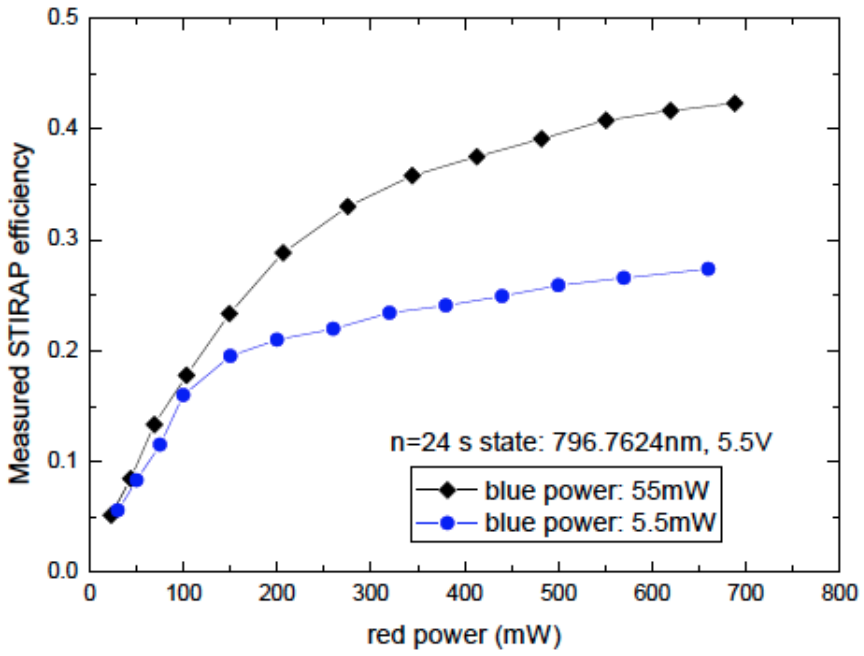

Figure 6.5: STIRAP efficiency of 24S state versus red light power outcome at blue power 5.5 mW and 55 mW.

24S state. Here the manifolds, as in Chapter 1, refer to the l mixing states due to the Stark splitting. As is shown in figure 6.6, the manifolds states tend to be less saturated. Before red light power reaches 700 mW, the same red light power induces smaller Rabi frequency of the manifolds states. Because the manifolds states have less transition strengths which corroborates with the deduction from Chapter 1 [11].

In higher red power region, the manifold states efficiency reaches maximum, too. From figure 6.5 we see that the trend shows that beyond 700 mW of red laser, the manifolds states will have a higher efficiency than the S state at the same power which is a contradiction to the "manifolds have less transition

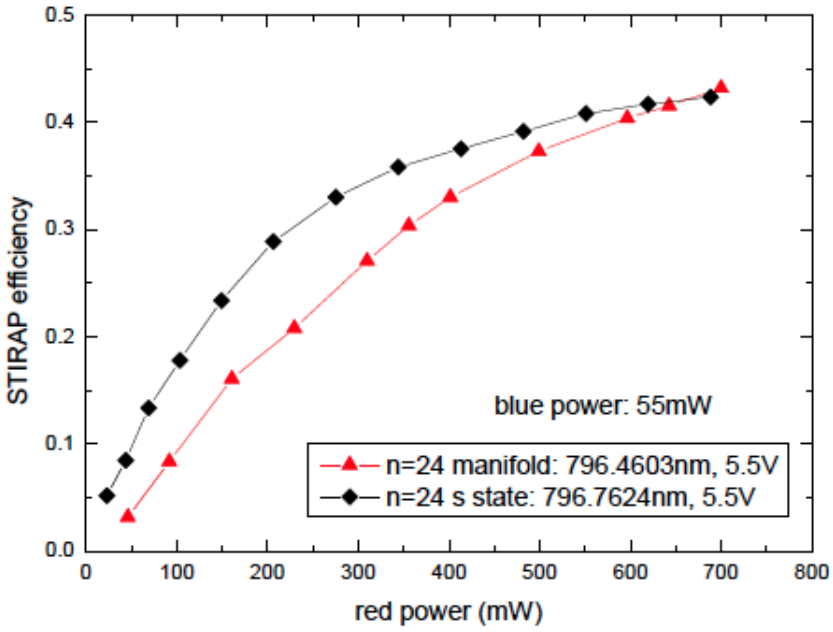

Figure 6.6: STIRAP efficiency of manifolds and S state versus red laser power. Blue laser power is fixed at 55 mW here [11].

strength" theory. The reason for this is that as we introduced before, both S state and manifolds state Rydberg atoms will decay along the path, and the S state will decay a lot faster than the manifolds [11]. This explains why the trend shows that manifold efficiency will be over the efficiency of the S state when red laser power is higher than 700 mW.

6.4.3 STIRAP Efficiency with Different Intermediate States

We may also vary the intermediate states (only the m sub-levels) in the STIRAP process, to see if there is any interference between different m states. Transitions from $^3S_1$ state to $^3P_{0,1,2}$ states are measured. Since we are going

to change blue light frequency to select different intermediate states that may cause the low efficiency, red laser frequency has to be tuned correspondingly to make sure we have the same final Rydberg state. As the transition strength between different ms may vary, we have to correspondingly change the lasers' intensities to compensate the Rabi frequency.

Figure 6.7 is a brief scheme of the transition process from $^3S_1$ to $^3P_{0,1,2}$. The numbers on the paths indicate the corresponding transition strengths [35]. From the selection rule $\Delta m = 0, \pm 1$, we can see the available paths for the transition to take are presented in figure 6.7. These are just potential paths and the polarization further selects which one the transition will take.

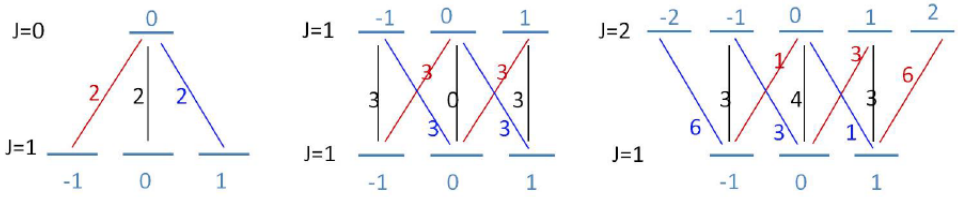

Figure 6.7: Transition strengths of different paths from state $^3S_1$ to $^3P_{1,2,3}$.

We first look in to the transition via intermediate state $^3P_0$. The metastable state atoms in $^3S_1$ are evenly distributed among the three states with different m values of $0, \pm 1$. So if we only use linearly polarized laser to drive the transition from $^3S_1, m = 0$ to $^3P_0, m = 0$, theoretically only one third of the population will get involved in the STIRAP process and be excited. This could be the reference of determining if there is any inter-level coupling between different ms.

Compare the number of paths available for equal ms for vertically polarized

light, we see there is only one for J=0 and three for J=2. Here we can use the knowledge we already obtained. We can measure the STIRAP efficiency of them and if there is any coupling between different m levels in the J=2 case, the measured efficiency should be lower than three times of the measurement result of J=0.

After compensating the laser wavelength and laser intensity we get a result [11] that the highest efficiency with respect to intermediate state of J=0 is roughly one third of the efficiency with respect to J=2. So far the highest J=0 efficiency is approximately 15%.

We can also measure the efficiency of J=1 state similarly with the blue frequency locked to it. From figure 6.7, we see that the transition from $^3\mathrm{S}_1, m = 0$ to $^3\mathrm{P}_1, m = 0$ is forbidden here. That is, two thirds of the total population can be potentially involved in the transition, and the excited population should be approximately 30% less than the $^3\mathrm{P}_2$ state. And the measurement result agrees well with this prediction [11]! And the efficiency for J=1 is $\sim 30\%$.

From here we can confirm that the interaction between different m levels should not be the reason that we can not achieve higher STIRAP efficiency. Because if it was, we would have observed an efficiency signal of J=2 state far lower than the signal of J=0. Since couplings between different m paths that only exist in J=2 state lower the efficiency is assumed. From another point of view, we should have observed a signal of J=0 state far more than one third of the signal of J=2 state if it was.

6.5 Transverse Velocity Distribution Induced Detunings

After measuring and ruling out all other possible reasons that may cause a low efficiency, we have put our attention to the transverse velocity spread of the atomic beam. As is discussed in Chapter 4, if the pump and Stokes lasers do not precisely match the resonance frequency, instead the they have a detuning from the resonance, the best efficiency that the STIRAP can achieve reduces from 1 to $1/\Omega_{eff}$. Ideally the STIRAP lasers should be perpendicular to the atomic beam as it is a "beam". That means all the atoms should travel and only travel longitudinally, whereas in our experiment, we can not guarantee that, or at least not perfectly. A transverse velocity spread in the atomic beam will cause Doppler shift to above or below resonance. As we can see in figure 6.8, atoms with different transverse velocity see different blue and red frequencies, causing Doppler shifts. As the STIRAP lasers can only be on resonance with a certain transverse velocity group (and we always want zero). A detuning is induced to both transitions of the atoms with a non-zero transverse velocity. What's more painful is that since the two lasers are co-propagating, the detunings can not compensate each other. The Dopper shifts will always be towards the same direction, causing the total detuning to be either above or below the resonance with the magnitude of the sum of the two individual Doppler induced detunings. In the future we plan to use counter propagating lasers to reduce the Doppler detuning. But right now we only have the best efficiency of no more than 50%

[12].

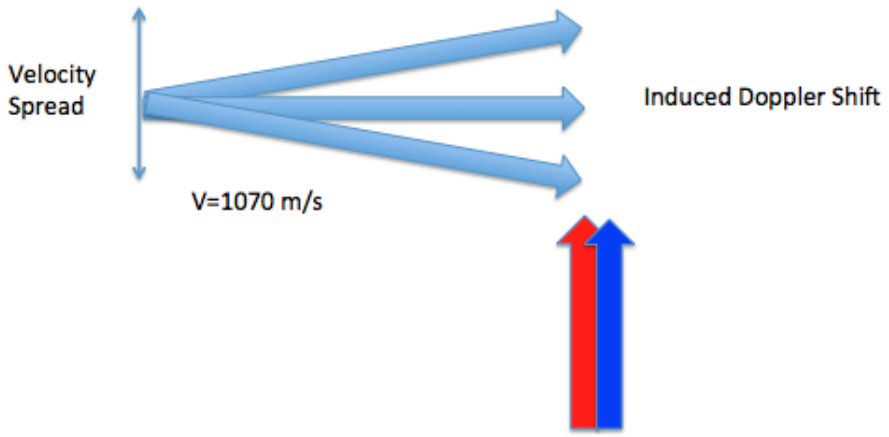

Figure 6.8: Transverse velocity spread induced Doppler shift. The atoms with different transverse velocities are not on resonance with the red and blue lasers but with a detuning. Which will cause a lowered STIRAP efficiency.

We may run a numerical calculation of the relative efficiency for different velocity groups by taking the detunings for each group into account. Set the pump and Stokes laser on resonance with the group with zero transverse velocity. Hence other groups will experience a detuning and their efficiency must be lower. Here we may just scan the red laser frequency across the Stark splitting range to match the transitions. As the simulation done by Yuan Sun [12]. As below in figure 6.9.

From above we see although ideally the STIRAP can get an efficiency of 100% for the zero transverse velocity group and the transverse velocity spread caused by Doppler detuning is still the main problem to get the STIRAP efficiency

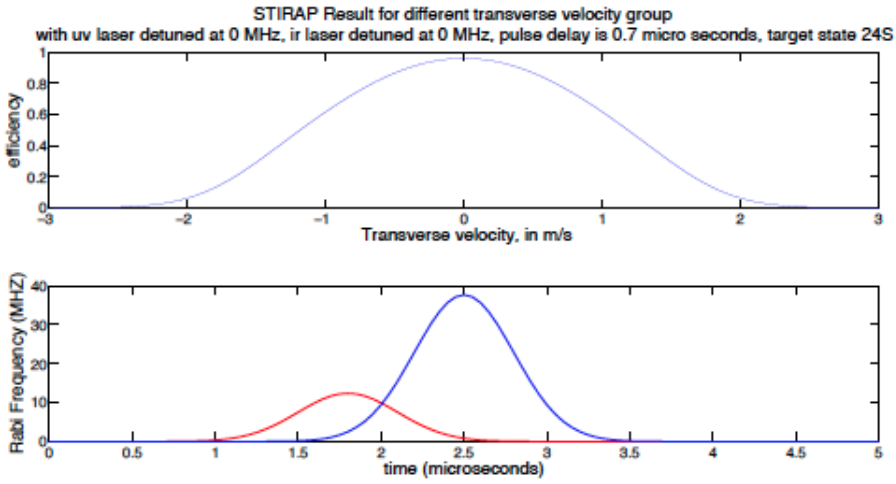

Figure 6.9: Numerical simulation result of the total efficiency of different transverse velocity groups. The lasers' Rabi frequencies are shown in the graph below [12].

higher. The second figure shows Rabi frequencies of the blue and red laser as a function of time. As we introduced in Chapter 2 the only tool we use to limit the transverse velocity spread is an aperture of 5 mm $\times$ 3 mm. In the future we expect the counter propagating lasers could make the two detunings partially neutralize each other and improve the whole efficiency.

Bibliography

[1] I. Estermann and S. N. Foner. History of molecular beam research: Personal reminiscences of the important evolutionary period 1919-1933. *American Journal of Physics*, 43:661–671, August 1975.

[2] T.W. Hansch and A.L. Schawlow. Cooling of gases by laser radiation. *Optics Communications*, 13(1):68 – 69, 1975.

[3] Peter J. Martin, Bruce G. Oldaker, Andrew H. Miklich, and David E. Pritchard. Bragg scattering of atoms from a standing light wave. *Phys. Rev. Lett.*, 60:515–518, Feb 1988.

[4] B. Friedrich and D. Herschbach. Stern and Gerlach: How a Bad Cigar Helped Reorient Atomic Physics. *Physics Today*, 56(12):53–59, December 2003.

[5] R. J. Cook and R. K. Hill. An electromagnetic mirror for neutral atoms. *Optics Communications*, 43:258–260, October 1982.

[6] V. I. Balykin and V. G. Minogin. Focusing of atomic beams by near-field atom microlenses: The bethe-type and the fresnel-type microlenses. *Phys. Rev. A*, 77:013601, Jan 2008.

[7] J G Kalnins, J M Amini, and H Gould. Focusing a fountain of neutral cesium atoms with an electrostatic lens triplet. *Phys. Rev. A*, 72(physics/0603127. LBNL-57137):043406. 8 p, Mar 2006.

[8] E. Urban, T. A. Johnson, T. Henage, L. Isenhower, D. D. Yavuz, T. G. Walker, and M. Saffman. Observation of Rydberg blockade between two atoms. *Nat Phys*, 5(2):110–114, February 2009.

[9] M. D. Lukin, M. Fleischhauer, R. Cote, L. M. Duan, D. Jaksch, J. I. Cirac, and P. Zoller. Dipole blockade and quantum information processing in mesoscopic atomic ensembles. *Phys. Rev. Lett.*, 87:037901, Jun 2001.

[10] Seung Hyun Lee. *Coherent Manipulation of Rydberg Helium Atoms in Inhomogeneous Electric Fields*. PhD thesis, SUNY Stony Brook, 2006.

[11] Xiaoxu Lu. *Excitation of Helium to Rydberg States Using STIRAP*. PhD thesis, SUNY Stony Brook, 2011.

[12] Yuan Sun. *Stimulated Raman Adiabatic Passage between Metastable and Rydberg States of Helium*. PhD thesis, SUNY Stony Brook, 2013.

[13] T.F.Gallagher. Rydberg atoms. *Reports on Progress in Physics*, 51(2):143, 1988.

[14] I. Martinson and L.J. Curtis. Janne rydberg his life and work. *Nuclear Instruments and Methods in Physics Research Section B: Beam Interactions with Materials and Atoms*, 235(14):17 – 22, 2005. The Physics of Highly Charged Ions Proceedings of the Twelfth International Conference on the Physics of Highly Charged Ions (HCI-2004) Twelfth International Conference on the Physics of Highly Charged Ions.

[15] III Olmsted, John. Excitation of nitrogen triplet states by electron impact. *Radiation Research*, 31(2):pp. 191–200, 1967.

[16] M. Haugh, T. G. Slanger, and K. D. Bayes. Electronic excitation accompanying charge exchange. *The Journal of Chemical Physics*, 44(2), 1966.

[17] Thomas F. Gallagher. *Rydberg Atoms*. Cambirdge University Press, 1994.

[18] The quantum defect. In *Topics in Atomic Physics*, pages 214–229. Springer New York, 2006.

[19] C.J.Foot. *Atomic Physics*. Oxford University Press, 2005.

[20] C-J Lorenzen and K Niemax. Quantum defects of the $n^2\mathrm{p}_{1/2,3/2}$ levels in 39k,i and 85rb,i. *Physica Scripta*, 27(4):300, 1983.

[21] Myron L. Zimmerman, Michael G. Littman, Michael M. Kash, and Daniel Kleppner. Stark structure of the rydberg states of alkali-metal atoms. *Phys. Rev. A*, 20:2251–2275, Dec 1979.

[22] J. Kawanaka, M. Hagiuda, K. Shimizu, F. Shimizu, and H. Takuma. Generation of an intense low-velocity metastable-neon atomic beam. *Applied Physics B*, 56(1):21–24, 1993.

[23] H. C. Mastwijk, J. W. Thomsen, P. van der Straten, and A. Niehaus. Optical collisions of cold, metastable helium atoms. *Phys. Rev. Lett.*, 80:5516–5519, Jun 1998.

[24] Claire Allred. *Neutral Atom Lithography with Metastable Helium.* PhD thesis, SUNY Stony Brook, 2009.

[25] Ole Bjarlin Jensen. Frequency doubling. Technical University of Denmark.

[26] P. A. Franken and J. F. Ward. Optical harmonics and nonlinear phenomena. *Rev. Mod. Phys.*, 35:23–39, Jan 1963.

[27] T.W. Hansch and B. Couillaud. Laser frequency stabilization by polarization spectroscopy of a reflecting reference cavity. *Optics Communications*, 35(3):441 – 444, 1980.

[28] D. A. Kleinman. Nonlinear dielectric polarization in optical media. *Phys. Rev.*, 126:1977–1979, Jun 1962.

[29] R.W.P. Drever, J.L. Hall, F.V. Kowalski, J. Hough, G.M. Ford, A.J. Munley, and H. Ward. Laser phase and frequency stabilization using an optical resonator. *Applied Physics B*, 31(2):97–105, 1983.

[30] R. V. Pound. Electronic frequency stabilization of microwave oscillators. *Review of Scientific Instruments*, 17(11), 1946.

[31] Eric D. Black. An introduction to pounddreverhall laser frequency stabilization. *American Journal of Physics*, 69(1), 2001.

[32] *Operators Manual of TIS-SF-777 CW single-frequency ring Ti:Sapphire laser.*

[33] K. Bergmann, H. Theuer, and B. W. Shore. Coherent population transfer among quantum states of atoms and molecules. *Rev. Mod. Phys.*, 70:1003–1025, Jul 1998.

[34] C.T.W. Lahaye, W. Hogervorst, and W. Vassen. Stark manifolds of barium rydberg states. *Zeitschrift fr Physik D Atoms, Molecules and Clusters*, 7(1):37–45, 1987.

[35] H. J. Metcalf and P. van der Straten. *Laser Cooling and Trapping.* Springer, 2002.

[36] I. I. Rabi. Space quantization in a gyrating magnetic field. *Phys. Rev.*, 51:652–654, Apr 1937.

[37] Bruce W. Shore. *The Theory of Coherent Atomic Excitation.* Wiley-VCH, 1990.

[38] Xiyue Miao. *Properties of Adiabatic Rapid Passage Sequences.* PhD thesis, SUNY Stony Brook, 2009.

[39] Daniel Stack. *Optical Forces from Periodic Adiabatic Rapid Passage Sequences in Metastable Helium.* PhD thesis, SUNY Stony Brook, 2012.

[40] F.T. Hioe and J.H. Eberly. N-Level Coherence Vector and Higher Conservation Laws in Quantum Optics and Quantum Mechanics. *Phys.Rev.Lett.*, 47:838–841, 1981.

[41] V.G. Minogin and O.T. Serimaa. Resonant light pressure forces in a strong standing laser wave. *Optics Communications*, 30(3):373 – 379, 1979.

[42] U. Gaubatz, P. Rudecki, S. Schiemann, and K. Bergmann. Population transfer between molecular vibrational levels by stimulated raman scattering with partially overlapping laser fields. a new concept and experimental results. *The Journal of Chemical Physics*, 92(9), 1990.

[43] WikiPedia. Rotating wave approximation, 2014.

[44] W. E. Cooke and T. F. Gallagher. Effects of blackbody radiation on highly excited atoms. *Phys. Rev. A*, 21:588–593, Feb 1980.

[45] T. F. Gallagher and W. E. Cooke. Interactions of blackbody radiation with atoms. *Phys. Rev. Lett.*, 42:835–839, Mar 1979.

[46] P.R. Koch, H. Hieronymus, A.F.J. Van Raan, and W. Raith. Direct observation of the interaction between rydberg atoms and blackbody radiation. *Physics Letters A*, 75(4):273 – 275, 1980.

[47] John W. Farley and William H. Wing. Accurate calculation of dynamic stark shifts and depopulation rates of rydberg energy levels induced by blackbody radiation. hydrogen, helium, and alkali-metal atoms. *Phys. Rev. A*, 23:2397–2424, May 1981.

[48] I. L. Glukhov, E. A. Nekipelov, and V. D. Ovsiannikov. Blackbody-induced decay, excitation and ionization rates for rydberg states in hydrogen and helium atoms. *Journal of Physics B: Atomic, Molecular and Optical Physics*, 43(12):125002, 2010.

[49] Xiaoxu Lu, Yuan Sun, and Harold Metcalf. Rydberg atom spectroscopy enabled by blackbody radiation ionization. *Phys. Rev. A*, 84:033402, Sep 2011.

[50] F. Robicheaux. Ionization due to the interaction between two rydberg atoms. *Journal of Physics B: Atomic, Molecular and Optical Physics*, 38(2):S333, 2005.

[51] Chris Corder. *Optical Forces on Metastable Helium*. PhD thesis, SUNY Stony Brook, 2014.

[52] J.H.Eberly L.Allen. *Optical Resonance and Two-Level Atoms*. Dover Publications, Inc., 1987.

[53] J. Soding, R. Grimm, Yu. B. Ovchinnikov, Ph. Bouyer, and Ch. Salomon. Short-distance atomic beam deceleration with a stimulated light force. *Phys. Rev. Lett.*, 78:1420–1423, Feb 1997.